J. Fluid Mech. (2007), *vol.* 593, *pp.* 405–452. © 2007 Cambridge University Press
doi:10.1017/S002211200700897X Printed in the United Kingdom

Surface gravity wave effects in the oceanic boundary layer: large-eddy simulation with vortex force and stochastic breakers

PETER P. SULLIVAN[1], JAMES C. McWILLIAMS[2] AND W. KENDALL MELVILLE[3]

[1]National Center for Atmospheric Research, Boulder, CO 80307, USA
[2]Department of Atmospheric and Oceanic Sciences and Institute of Geophysics and Planetary Physics, UCLA, Los Angeles, CA 90095-1565, USA
[3]Scripps Institution of Oceanography, University of California, San Diego, La Jolla, CA 92093-0213, USA

(Received 6 October 2006 and in revised form 30 August 2007)

The wind-driven stably stratified mid-latitude oceanic surface turbulent boundary layer is computationally simulated in the presence of a specified surface gravity-wave field. The gravity waves have broad wavenumber and frequency spectra typical of measured conditions in near-equilibrium with the mean wind speed. The simulation model is based on (i) an asymptotic theory for the conservative dynamical effects of waves on the wave-averaged boundary-layer currents and (ii) a boundary-layer forcing by a stochastic representation of the impulses and energy fluxes in a field of breaking waves. The wave influences are shown to be profound on both the mean current profile and turbulent statistics compared to a simulation without these wave influences and forced by an equivalent mean surface stress. As expected from previous studies with partial combinations of these wave influences, Langmuir circulations due to the wave-averaged vortex force make vertical eddy fluxes of momentum and material concentration much more efficient and non-local (i.e. with negative eddy viscosity near the surface), and they combine with the breakers to increase the turbulent energy and dissipation rate. They also combine in an unexpected positive feedback in which breaker-generated vorticity seeds the creation of a new Langmuir circulation and instigates a deep strong intermittent downwelling jet that penetrates through the boundary layer and increases the material entrainment rate at the base of the layer. These wave effects on the boundary layer are greater for smaller wave ages and higher mean wind speeds.

1. Introduction

The air–sea interface and more broadly the ocean mixed layer (or ocean boundary layer, OBL) plays an important role in geophysical flows. It modulates air–sea fluxes in the global ocean circulation (Large, McWilliams & Doney 1995; McWilliams 1996), and in the most extreme environment controls tropical cyclone intensity (Emanuel 2004). The ocean surface layers support air–sea fluxes, surface gravity waves, boundary-layer turbulence, Ekman currents and significant air (gas) entrainment when the surface is disrupted by intermittent breaking waves. Despite the differences in length scales O(1 mm–100 m) and time scales O(1 ms–1 h), the physics of these phenomena are closely linked. Progress by direct computational methods has been

https://doi.org/10.1017/S002211200700897X Published online by Cambridge University Press

impeded by the structural complexity of upper-ocean flows, disparity in magnitude and time scales among the flow components, and by high Reynolds numbers Re. The current generation of bulk (ensemble average) computational models of the OBL used in large-scale prediction codes does not account for the dynamic nature of the surface wave field. These 1-D (vertical column) parameterizations of the OBL (e.g. Mellor & Yamada 1982; Large *et al.* 1995; Price, Weller & Pinkel 1986) use vertical mixing rules partially based on past experience with the atmospheric boundary layer and laboratory experiments. This perception of the OBL has been, in part, a practical necessity as the hostile measuring environment does not permit easy probing of the important interactions that determine the turbulent fluxes of momentum, scalars and energy across the temporally and spatially evolving air–sea interface. While many aspects of surface waves are well known, a clear understanding of their relationship to fluxes, turbulence and currents has long been elusive. However, the impact of waves on OBL dynamics is acknowledged in more recent bulk models (e.g. Craig & Banner 1994; McWilliams & Sullivan 2000; Smyth *et al.* 2002; Kantha & Clayson 2004; Lewis & Belcher 2004; Melsom & SÆtra 2004; Ardhuin & Jenkins 2006; Rascale, Ardhuin & Terray 2006), with improvements motivated by better measurements and results from turbulence-resolving simulations with wave effects as described here.

The technique of large-eddy simulation (LES) calculates the currents and turbulence in response to the fluxes using an embedded model for subgrid-scale turbulent mixing and dissipation. Relatively recently, the wave influences associated with Stokes drift $\boldsymbol{u}^{St}$ (i.e. vortex force and Lagrangian material transport) have been incorporated in LES (Skyllingstad & Denbo 1995; McWilliams, Sullivan & Moeng 1997; Polton, Lewis & Belcher 2004; Li, Garrett & Skyllingstad 2005). These influences represent conservative wave–current interactions averaged over the more rapid wave fluctuations (Craik & Leibovich 1976; McWilliams & Restrepo 1999; McWilliams, Restreppo & Lane 2004). Their effect is to induce coherent Langmuir circulations in the OBL turbulence that importantly modify the resulting mixing, dissipation and Ekman current profile. In shallow water, depth-filling Langmuir cells also play important roles in sediment transport (Gargett, Tejada-Martínez & Grosch 2004). Thorpe (2004, 2005) provides recent reviews of Langmuir circulations and their role in upper ocean dynamics. We note that low-Reynolds number direct numerical simulation (DNS) and LES have previously been used to examine turbulent water flows, namely free-surface flows and stress-driven interfaces, where the wave amplitudes and/or the wave phase speeds are small compared to those considered here (e.g. Enstad, Nagaosa & Alendal 2006; Tsai 1998; Tsai & Yue 1996).

Intermittent wave breaking is also important in this regime, but it has rarely been included in oceanic LES. Craig & Banner (1994) represented breaking as a surface flux of turbulent kinetic energy which enhances mixing and dissipation rates near the surface in a Reynolds-averaged boundary-layer model, and Noh, Min & Raasch (2004) verified these effects in LES. Furthermore, breaking waves transfer momentum from the wind-generated wave field to the oceanic turbulence and currents; this is the dominant mechanism for the net momentum exchange between winds and currents usually associated with the wave-averaged surface wind stress (Donelan 1998; Banner & Peirson 1998). The conventional LES practice is to specify a mean surface stress $\boldsymbol{\tau}$. However, this does not adequately represent the intermittent injection of momentum and energy from the wave field by breaking. An alternative LES representation of breaking that captures both energy and momentum injection (Sullivan, McWilliams & Melville 2004) is a random field of near-surface impulses whose attributes are designed to match field and laboratory observations of breaking waves (e.g. Rapp

https://doi.org/10.1017/S002211200700897X Published online by Cambridge University Press

& Melville 1990; Melville & Matusov 2002; Melville, Veron & White 2002) and the mean fluxes of momentum and energy.

This paper reports LES for the OBL with both types of wave effects predominantly for approximate equilibrium, or 'fully-developed', conditions among the wind, waves and currents. However, we also show that the qualitative effects of the wave processes are retained for smaller wave ages, or fetch-limited conditions. For a given mean wind $\boldsymbol{U}_a$ (e.g. the wind at the height $z = 10$ m) and sufficiently large fetch, the wave field comes into a fully-developed wavenumber-spectral distribution for, say, the sea-surface elevation, with generation by wind form stress balancing loss by breaking integrated over the spectrum. The elevation spectrum implies a mean Stokes drift profile $\boldsymbol{u}^{St}(z)$, and the breaker spectrum implies a probability distribution function for the random impulses. The impulse distribution is normalized to have the equivalent integrated current acceleration expected from the empirical bulk formula relating the mean wind and wind stress $\boldsymbol{\tau}$, as well as an energy input equivalent to the empirical kinetic energy loss rate from the waves. Thus, the impulses can wholly replace $\boldsymbol{\tau}$ in the conventional LES formulation and be a more faithful representation of the true mechanisms of air–sea momentum and energy fluxes through the wave field.

Our results exhibit a subtle interplay between the vortex force and breaking. Langmuir circulations intensify the surface vorticity and enhance turbulent transport throughout the boundary layer into the underlying entrainment zone. Breakers enhance the near-surface mixing, destroy the Monin–Obhukov similarity structure, provide seed vorticity for wave–current (CL2, Leibovich 1983) instabilities, and limit the spatial extent of the Langmuir circulations. Under certain circumstances breaker responses and Langmuir circulations combine to make strong intermittent downward jets that further enhance the vertical transport efficiency.

Section 2 presents the representation of wind and waves in near-equilibrium conditions. Section 3 presents the stochastic breaker model. Section 4 is the LES model formulation. Section 5 describes the experimental design. Section 6 is an analysis of a primary experiment with $U_a = 15$ m s^{-1}. Section 7 analyses model sensitivities, especially to wind speeds up to a value of $U_a = 30$ m s^{-1}, and wave age. Finally, § 8 is a summary and discussion.

2. Winds and waves approaching equilibrium

For modeling wave effects in the ocean mixed layer, we must specify both the wave spectrum to determine the profile of Stokes drift and the distribution (spectrum) of breaking waves for transfer of momentum and kinetic energy to the underlying water column. In both cases, our primary interest is the situation approaching wind–wave equilibrium where the wave spectrum is well developed and the atmospheric inputs of momentum and energy flux are perhaps best characterized by observations. Full development refers to an asymptotic state in which the energy density, the peak frequency and the shape of the wave spectrum are changing very slowly with time following synoptic changes in the wind. We neglect the portion of wind input which goes into bulk wave growth in the action balance equation (Komen *et al.* 1994, p. 47) and always adopt the leading-order balance of wind input equal to dissipation by breaking. Phillips (2002) has developed a theoretical model for the unsteady influence of waves on Langmuir circulations.

Apart from overall equilibrium between wind and waves, or full-development, an equilibrium subrange in a developing wind–wave spectrum may also exist. This subrange corresponds to the region in which the sum of the wind input, nonlinear

https://doi.org/10.1017/S002211200700897X Published online by Cambridge University Press

wave–wave interactions and the dissipation, mainly due to breaking, are in balance (Phillips 1985).

2.1. *Wave spectra and Stokes drift*

The vertical profile of Stokes drift $u^{St}(z)$ is a primary input to OBL models that incorporate wave-averaged effects (e.g. McWilliams *et al.* 1997; Kantha & Clayson 2004). Past LES typically estimate $u^{St}(z)$ from monochromatic wave fields (Skyllingstad & Denbo 1995; McWilliams *et al.* 1997; Noh *et al.* 2004) chosen to approximate a dominant component in the wave spectrum (the work described by Polton *et al.* (2004) is an exception). In the case of wind–wave equilibrium, measurements of the wave spectrum are more complete and thus we can be more precise with the specification of the Stokes profile. Recently, Alves, Banner & Young (2003) revisited the classical Pierson–Moskowitz wave-height spectrum (Pierson & Moskowitz 1964) for fully-developed seas, reanalysing the original database to refine the spectral shape and the integral parameters that quantify the spectrum. A database of 29 events was interrogated to establish the spectral shape and fitting constants. Adhering to the spectral shape proposed by Donelan, Hamilton & Hui (1985), Alves *et al.* (2003) favor the empirical spectral form,

$$F(f) \;=\; \frac{\alpha_w\, g^2}{(2\,\pi)^4\, f^4\, f_p} \exp\left[-\left(\frac{f}{f_p}\right)^{-4}\right], \tag{2.1}$$

where $f = \sigma/2\pi$ is the frequency, σ is the radial frequency, α_w is the 'Phillips constant', g is the gravitational acceleration and f_p is the peak in the spectrum related to a reference atmospheric wind $U_a(z = 10\ \mathrm{m})$ by

$$\nu \;=\; f_p\, U_a/g. \tag{2.2}$$

Empirical constants that appear in the above expressions are $\nu \approx 0.123$ and $\alpha_w \approx 6.15 \times 10^{-3}$. The observations of significant wave height, $H_s = 4\langle\eta^2\rangle^{1/2}$, where $\langle\eta^2\rangle$ is the variance of the surface displacement due to the waves, closely follow the curve fit

$$H_s \;=\; 0.24\, U_a^2/g\,. \tag{2.3}$$

The wave energy density $E = \rho_o g\langle\eta^2\rangle$, where ρ_o is the density of the water. The phase speed at the peak of the equilibrium wave height spectrum is $c_{p,E} = U_a/2\pi\nu$. Thus the phase speed at the peak is moving about 20% faster than the reference wind in fully-developed conditions. The linear dispersion relationship $c^2 = g/k$ along with $f = g/2\pi\, c$ is used to move between frequency f, wavenumber k and phase speed c spaces. The observations that are used to determine the wave spectral shape and constants extend out to $f/f_p \approx 4$.

McWilliams & Restrepo (1999, equation 62), using the procedure outlined by Kenyon (1969), show how to incorporate a full wave spectrum in the estimate of u^{St}. For our LES (§4), we follow this approach and employ numerical quadrature to evaluate

$$u^{St}(z) = \frac{2}{g}\int_0^\infty F(\sigma)\,\sigma^3 \exp\left[\frac{2\sigma^2 z}{g}\right] \mathrm{d}\sigma\,. \tag{2.4}$$

The main difference between the Alves–Donelan wave spectrum, given by (2.1), and the Pierson–Moskowitz formula is that the former decays at a slower rate at high frequencies, f^{-4} compared to f^{-5}. This slope change has no influence on u^{St} for $z < -2$ m, but for $z = [-2, 0]$ m the Alves–Donelan spectrum generates a sharper near-surface gradient in the Stokes profile compared to that obtained from

https://doi.org/10.1017/S002211200700897X Published online by Cambridge University Press

the Pierson–Moskowitz wave spectrum. A high-frequency tail with slope f^{-5} can be appended to the spectral shape given by (2.1) to extend its range of applicability (e.g. Banner 1990; Terray *et al.* 1996).

2.2. *Bulk atmospheric inputs of momentum and energy*

At wind speeds above (6–8) m s^{-1}, the wave field is the main transmitter of atmospheric momentum and energy passing nearly 100% of these fluxes locally to the underlying currents (Terray *et al.* 1996; Donelan 1998, 2001) primarily through the action of wave breaking. Thus the global amount of momentum and energy that is available to generate currents from breaking is known based on the atmospheric inputs. The bulk aerodynamic method is most often used to determine the momentum flux in the atmospheric surface layer. There is debate about the empirical constants appearing in the formula

$$\boldsymbol{\tau}_a = \rho_a C_d |\boldsymbol{U}_a| \boldsymbol{U}_a \,, \tag{2.5}$$

but this functional form is generally well accepted. Here ρ_a is the air density, U_a is the mean wind at the reference height $z = 10$ m, and C_d is a wind speed dependent drag coefficient. The atmospheric friction velocity is then $u_{*a} = \sqrt{|\boldsymbol{\tau}_a|/\rho_a}$. For our purposes we adopt the drag parameterization of Liu, Katsaros & Businger (1979),

$$C_d = \begin{cases} 1.3 \times 10^{-3} \,, & U_a \leqslant 10 \text{ m s}^{-1} \\ (0.79 + 0.0509 \times U_a) \times 10^{-3}, & U_a \geqslant 10 \text{ m s}^{-1} \end{cases} \tag{2.6}$$

noting other prescriptions are available (e.g. Large & Pond 1982; Donelan 1998; Fairall *et al.* 2003) that include the effects of finite fetch and the state of wave development (or wave age). Observations indicate that the linear variation of C_d with wind speed continues up to about 25–30 m s^{-1}. For even higher winds there are few field measurements (Powell, Vickery & Reinhold 2003), but both field and laboratory data show that the drag coefficient saturates, or reaches a weak maximum, around $C_d \approx 2.3 \times 10^{-3}$ at wind speeds around 30–35 m s^{-1} (Donelan *et al.* 2004). The causes of this regime change in C_d near the threshold for hurricane winds are a topic of current research since the maximum intensity of hurricanes depends on the ratio of the coefficients of momentum to enthalpy transfer across the air–sea interface (Emanuel 2004).

Breaking waves supply momentum for current generation but also serve as a significant source of kinetic energy for the water column. Our wave–OBL coupling accounts for the energy flux flowing from winds to waves to currents. There are no direct measurements of energy flux $\mathcal{E}_a$ from the atmosphere to the wave field and thus an alternative method is required to determine this variable. Terray *et al.* (1996) propose the parameterization

$$\mathcal{E}_a = |\boldsymbol{\tau}_a| \hat{c} \,, \qquad \text{where} \quad \hat{c} = u_{*a}\, g_t(c_p/u_{*a}) \,, \tag{2.7}$$

based on a wave-growth model developed by Donelan & Pierson (1987). In this expression $\hat{c}$ is an 'effective phase speed', a velocity scale characteristic of the wave field, and it reflects contributions over the entire wave spectrum. Based on six different observational datasets, Terray *et al.* (1996, figure 8) find that $\hat{c}/u_{*a}$ (or g_t) depends critically on the state of wave development. We adopt wave age, defined as the ratio of the phase speed at the peak of the wave spectrum to the atmospheric friction velocity c_p/u_{*a}, as a bulk measure of wave development. g_t is in the range 3–4 for waves approaching full development ($c_p/u_{*a} \approx 30$), attains a maximum of about 7–9 for developing seas ($c_p/u_{*a} = 15$–20), and falls to small values approximately 1–4 for

https://doi.org/10.1017/S002211200700897X Published online by Cambridge University Press

very young waves ($c_p/u_{*a} < 10$). The explicit conversion between wave age c_p/u_{*a} and Terray parameter g_t used in the present work is given in table 1 in § 5. Terray *et al.* (1996) find that dissipation measurements taken beneath breaking waves, when scaled by the wind input $\mathcal{E}_a$ and significant wave height H_s, collapse their data over a range of growing waves $4.3 < c_p/u_{*a} < 7.4$. Further support for the energy flux parameterization (2.7) is provided by Drennan *et al.* (1996) as they show this form also appears to apply for larger wave ages closer to wind–wave equilibrium. Phillips (1985) (see also Melville 1994) has developed an equilibrium model for atmospheric energy flux based on breaking statistics that is functionally different from the proposal by Terray *et al.* (1996), but its predictions are in general agreement with (2.7). In the absence of additional information, we adopt (2.7) as our prescription of the atmospheric energy flux and consider the impacts of wave age in a limited range approaching equilibrium $c_p/u_{*a} = (19–30)$.

As a consistency check we note that in the absence of other external energy sources the vertically integrated dissipation rate in the water is approximately equal to the average energy flux $\mathcal{E}_a$ from winds to waves:

$$\mathcal{E}_a/\rho_o \approx \int_{-\infty}^{0} \epsilon \, \mathrm{d}z \,, \tag{2.8}$$

where ϵ is the local dissipation rate per unit of water mass and z extends over the depth of the water column. This integral balance is in accord with the basic assumption that breaking is the dominant energy source (Terray *et al.* 1996). In our simulations we use (2.8) as an indicator of flow stationarity and global conservation of energy between the atmospheric inputs and dissipation in the water column. However, the LES also includes current shears, stratification and Stokes drift effects that further increase the dissipation in the water in addition to the contributions from breaking waves.

At this point, notice that the specification of the wave fields, Stokes drift and fluxes of momentum and energy can all be expressed in terms of the reference atmospheric wind. Hence the primary atmospheric input to our LES model of the OBL is U_a. Developing seas are parameterized by wave age as well as wind speed.

3. Stochastic breakers

The other physical process we wish to capture in our modeling is the intermittent and dynamical influences of breaking waves. Breaking encompasses a wide range of scales and is sufficiently complex that we must idealize this process, retaining its essential ingredients. First, we assume that the onset of breaking–which is likely linked to the local winds, wave–wave and wave–current interactions (Melville 1996)–is a random process uniformly distributed in space and time. This is consistent with the visual appearance of the broken sea surface under high wind conditions. However, it is also well known that the incidence of large-scale breaking is related to the group structure of the surface wave field, in an, as yet, not fully understood way (Donelan, Longuet-Higgins & Turner 1972). In the present formulation the averaging is over time scales much larger than the characteristic time of the wave groups, so any departure from an assumption of random incidence of breaking is not justified. Secondly, we represent an individual breaker as a compact function in space and time that captures the (average) bulk impulse from breaking (Sullivan *et al.* 2004). This avoids the considerable complexity of a full air–water simulation that cannot simultaneously span the range of scales from bubbles to mixed-layer turbulence. Also,

https://doi.org/10.1017/S002211200700897X Published online by Cambridge University Press

the imposed breaking impulses are assumed to be non-interacting, which allows a field of breakers to be built from a linear superposition of discrete events.

3.1. *Momentum transfer from waves to currents*

The wave field is an intermediate reservoir that releases momentum to the underlying water in localized intermittent impulses, and the primary path to current generation is through wave breaking. The momentum passed to the OBL is then a summation of randomly occurring breaking events. In our modeling the acceleration from a single event has only horizontal components,

$$\boldsymbol{A}^m \;=\; \mathscr{A}^m(\boldsymbol{x}, t, c^m)(\hat{\boldsymbol{x}}\cos\Theta^m + \hat{\boldsymbol{y}}\sin\Theta^m)\,, \tag{3.1}$$

where Θ^m is the breaker's angle of orientation in the LES coordinate system and $\mathscr{A}^m$ is our parameterization of the local space-time structure of acceleration amplitude for a single event in terms of its phase speed, c^m, and initiating location and time, $(\boldsymbol{x}^m, t^m)$ (§ 3.2). The breaker's phase speed vector is $\boldsymbol{c}^m = c^m(\hat{\boldsymbol{x}}\cos\Theta^m + \hat{\boldsymbol{y}}\sin\Theta^m)$. A single event provides momentum

$$\mathscr{M}^m(c^m, \Theta^m) = \rho_o \int_0^{T(c^m)} \int_0^{V(c^m)} \boldsymbol{A}^m(\boldsymbol{x}, t, c^m, \Theta^m)\, \mathrm{d}\boldsymbol{x}\, \mathrm{d}t \tag{3.2}$$

with magnitude

$$|\mathscr{M}^m| \;=\; \rho_o \int_0^{T(c^m)} \int_0^{V(c^m)} \mathscr{A}^m(\boldsymbol{x}, t, c^m)\, \mathrm{d}\boldsymbol{x}\, \mathrm{d}t\,. \tag{3.3}$$

The integration limits reflect the compact duration of breaking over space and time relative to the initiating coordinates, i.e. the impulse is non-zero over the period, $T(c)$, and volume, $V(c)$, of the breaking wave.

The total momentum supplied to the currents is the integrated effect of many randomly occurring breaking events of varying size, speed and orientation,

$$\boldsymbol{M}_b \;=\; N \int^{\Theta} \int^{c} \mathscr{M}(c, \Theta)\, c\, \mathscr{P}(c, \Theta)\, \mathrm{d}c\, \mathrm{d}\Theta\,. \tag{3.4}$$

In this expression, N is the total number of breakers and $\mathscr{P}(c, \Theta)$ is the probability density function (PDF) of breaker speeds c with orientation Θ and is normalized according to the definitions,

$$P(c) \;=\; \int^{\Theta} c\, \mathscr{P}(c, \Theta)\, \mathrm{d}\Theta, \qquad \text{where} \qquad \int^{c} P(c)\, \mathrm{d}c \;= 1\,. \tag{3.5}$$

N and $\mathscr{P}(c, \Theta)$ are functions of the environmental conditions, in particular wind speed and wave age (e.g. Wu 1988; Gemmrich & Farmer 1999; Melville & Matusov 2002).

Momentum conservation between atmosphere and ocean limits the total amount of momentum that can be passed through the wave field. The long-time, large-area total momentum conservation rule expressed in terms of the horizontal momentum flux, $\boldsymbol{\tau}_a$, from the atmosphere over an area of surface water, $\mathscr{S}$, and time period, $\mathscr{T}_p$, is

$$\boldsymbol{\tau}_a\, \mathscr{S}\, \mathscr{T}_p \;=\; \boldsymbol{M}_b\,, \tag{3.6}$$

where $\boldsymbol{M}_b$ is the momentum transferred by a field of breakers. Substitution of (3.4) into (3.6) connects the bulk atmospheric momentum to the probability of breaking and also defines a critical breaking parameter in the LES. We define the *average* rate

https://doi.org/10.1017/S002211200700897X Published online by Cambridge University Press

of breaker generation as

$$\dot{N} = \frac{N}{\mathscr{S}\mathscr{T}_p}, \tag{3.7}$$

where $\dot{N}$ is the number of breakers created per unit of water surface area per unit of time (units of s^{-1} m^{-2}). In other words, a sufficient number of breakers N at the proper scale must be created at a rate $\dot{N}$ to match the long-time large-area average of momentum (and energy) transfer in air and water given by (3.6). It is expected that $\dot{N} = \dot{N}(U_a, c_p/u_{*a})$.

Breaking releases momentum to generate currents but also energizes the water column, which is vividly apparent from images of breaking in the laboratory and in the field. Thus our modeling also needs to account for energy transfer from winds to waves to currents. From consideration of the reduction in momentum and energy densities of the wave field due to breaking (Phillips 1977), the total (kinetic and potential) energy released by an event is $\boldsymbol{c}^m \cdot \boldsymbol{\mathscr{M}}^m$ (Phillips 1985). This is consistent with the measurements of Terray *et al.* (1996), is similar to that used in second-order closure parameterizations (Craig & Banner 1994) and is consistent with our parameterization for breaker momentum†. By analogy with (3.4) and (3.6) the total energy transferred by a field of breakers is then

$$E_b = N \int^{\Theta} \int^{c} \boldsymbol{c} \cdot \boldsymbol{\mathscr{M}}(c, \Theta)\, c\, \mathscr{P}(c, \Theta)\, \mathrm{d}c\, \mathrm{d}\Theta\,. \tag{3.8}$$

Matching the atmospheric energy flux from winds to waves requires

$$\mathscr{E}_a \mathscr{S} \mathscr{T}_p = E_b\,. \tag{3.9}$$

3.2. *Momentum impulse from a single breaker*

The breaker model used here (Sullivan *et al.* 2004) is based on laboratory measurements by Rapp & Melville (1990), Loewen & Melville (1990), Melville *et al.* (2002) and video imagery of breaking in the field (Melville & Matusov 2002). The main results of the laboratory experiments are that: the duration of active breaking is $O(T)$; the maximum fluid velocity during breaking is $O(c)$; and the depth of penetration of the broken fluid is $O(2a)$, where T, c and a, are the characteristic period, linear phase speed and amplitude, respectively, of the breaking wave. The laboratory experiments also show that the post-breaking flow variables scale with the pre-breaking variables even at large times. We refer to this set of dimensional estimates as Froude scaling of breaking, with length and time scales related through the linear dispersion relationship. It is the basis of our formulation of the breaking model.

It may seem curious that a strongly nonlinear process such as breaking can be scaled using a linear dispersion relationship. However, there are some rather strong constraints on the theoretical maximum and empirical maximum phase velocities for surface gravity waves, and it is the phase velocity that relates the length and time scales. The maximum phase speed for nonlinear surface gravity waves is 9% larger than the linear phase speed and occurs at a wave slope of 0.436, slightly less than the slope of 0.443 for the Stokes limiting wave (Longuet-Higgins 1975). However, in practice fast instabilities and breaking tend to limit the maximum practical wave

† At low winds breaking is less obviously the dominant air–sea transfer process. Our breaker representation is thus relevant to the wind regime with U_a greater than about 5 m s^{-1} (Makin, Kudryavtsev & Mastenbroek 1995; Banner & Peirson 1998).

https://doi.org/10.1017/S002211200700897X Published online by Cambridge University Press

slope to 0.3, for which the corresponding steady wave phase velocity is just 5% larger than the linear phase speed. Thus for breaking kinematics, the use of the linear phase speed may involve errors of around 5%. For the dynamics, where the breaking momentum and energy fluxes scale as the fourth and fifth powers of the phase speed (Phillips 1985), the errors for individual breaking events may be up to 22% and 28%, respectively. However, the number of breakers is constrained to satisfy the bulk fluxes, so in this model, errors will flow through to the breaking statistics. Given the order of magnitude scatter in observations of breaking statistics, any errors in the scaling are within the scatter of the current observations.

The formula for an individual breaker impulse is

$$\mathscr{I} = \int_0^\infty \mathscr{A}\, \mathrm{d}t, \tag{3.10}$$

where

$$\mathscr{A} = k_b \frac{g}{2\pi} \mathscr{T}(\alpha)\, \mathscr{X}(\beta)\, \mathscr{Y}(\delta)\, \mathscr{Z}(\gamma)\,, \tag{3.11}$$

with the $(\mathscr{T}, \mathscr{X}, \mathscr{Y}, \mathscr{Z})$ space-time shape functions that are determined from DNS of a single isolated breaker designed to replicate the laboratory results of Melville *et al.* (2002). All breakers are assumed to be self-similar and separable in dimensionless time and space coordinates,

$$\begin{aligned} \alpha &= \frac{t - t_o}{T}\,, \qquad & \beta &= \frac{x - x_o}{c(t - t_o)}\,, \\ \delta &= \frac{2(y - y_o)}{\lambda}\,, \qquad & \gamma &= \frac{z}{\chi c(t - t_o)}\,, \end{aligned} \tag{3.12}$$

with $(t_o, x_o, y_o, z_o = 0)$ the onset time and position of the chosen breaker; (c, λ, T) are its phase speed, wavelength and period. The wave characteristics (c, λ, T) are related to each other through the deep-water linear dispersion relation $c^2 = g\lambda/2\pi$ with $T = \lambda/c$. Notice that in the normalized vertical coordinate (3.12) the constant $0 < \chi < 1$, which is just the aspect ratio of the depth to length of the breaker, controls the depth penetration of the breaker forcing; $\chi = 0.2$ matches the laboratory measurements of Melville *et al.* (2002). The specific functional forms for the shape functions is the set of equations (3.3) given in Sullivan *et al.* (2004). The momentum supplied by our breaking model (3.11) varies with wave phase speed c because of the explicit dependences in (3.12). If we substitute the model (3.11) for $\mathscr{A}$ into (3.3) for breaker momentum and convert the time and space integrations $\mathrm{d}\boldsymbol{x}\, \mathrm{d}t \to \mathrm{d}\beta\, \mathrm{d}\delta\, \mathrm{d}\gamma\, \mathrm{d}\alpha$ we find the breaker momentum increases rapidly with phase speed, i.e. $\boldsymbol{\mathscr{M}}(c) \sim c^7$. Similarly the breaker energy grows as c^8. These power-law dependences impact the determination of the breaker PDF.

3.3. *Breaker PDF*

Bulk conservation of momentum and energy fluxes between the atmosphere and ocean constrains the properties of the breaker field. Given $\mathcal{E}_a \mathscr{S}\mathscr{T}_p = E_b$ and $\boldsymbol{\tau}_a \mathscr{S}\mathscr{T}_p = \boldsymbol{M}_b$ and atmospheric inputs the unknowns are then the distribution of breakers across c (here the PDF of c) and the breaker generation rate. N is first eliminated by forming the energy–momentum flux ratio,

$$\mathcal{E}_a / |\boldsymbol{\tau}_a| \;=\; E_b / |\boldsymbol{M}_b|\,. \tag{3.13}$$

Substitution of the parameterization for atmospheric energy flux, given by (2.7), and the definitions of breaker momentum and energy, given by (3.4) and (3.8), into (3.13)

https://doi.org/10.1017/S002211200700897X Published online by Cambridge University Press

leads to

$$u_{*a}\, g_t \int^{\Theta} \int^{c} |\boldsymbol{\mathcal{M}}(c,\Theta)|\, c\, \mathcal{P}(c,\Theta)\, \mathrm{d}c\, \mathrm{d}\Theta \;=\; \int^{\Theta} \int^{c} \boldsymbol{c}\cdot\boldsymbol{\mathcal{M}}(c,\Theta)\, c\, \mathcal{P}(c,\Theta)\, \mathrm{d}c\, \mathrm{d}\Theta\,. \tag{3.14}$$

Equation (3.14) is a weak global constraint on the breaker PDF. The distribution of (discrete) breakers with phase speed and direction is unknown and additional information is needed to develop a specific computational form for $P(c,\Theta)$. Quantifying the distribution and magnitude of breakers in the field is a challenging observational task and as a result the wave-breaking dissipation spectrum remains the least understood term in the wave-action equation used in numerical wave forecasting (Komen *et al.* 1994; Donelan 2001). Recently, Melville & Matusov (2002) and Gemmrich (2005) attempted to measure breaking statistics using video imagery from an aircraft and a floating instrument platform (R/P FLIP), respectively. These measurements were partly motivated by the theoretical work of Phillips (1985) that proposes breaking statistics can be built from $\Lambda(c)\mathrm{d}c$, the average length of breaking crests per unit area of ocean surface traveling at velocities in the range $(c, c+\mathrm{d}c)$. Digitized video output supplies data on the distribution of $\Lambda(c)$, moments of $\Lambda(c)$ (corresponding to momentum and energy flux from waves to currents), directional distribution of breakers, as well as other statistics. The video measurement technique relies on imaging active whitecaps: breakers with visible air entrainment. Breakers generating few bubbles or foam are missed by the detection algorithms leading to an underestimate of small-scale breaking. Melville & Matusov (2002) estimate the small-scale resolution in their observations to be $\lambda \approx 0.7$ m corresponding to a phase speed $c \approx 1$ m s^{-1}. An important result from this dataset shows an exponential decrease of $\Lambda(c)$ with c and a variation of $\Lambda(c)$ as wind speed cubed over the range of wind speeds 7.2–13.6 m s^{-1}.

A direct connection between the PDF of breaking that appears in (3.14) and measurements of $\Lambda(c)$ depends on multiple unknown factors, including the model for breaker momentum transfer. Given this ambiguity we make two assumptions: (I) we neglect the directional distribution of breakers and assume alignment between the surface winds and breakers noting that this dependence can easily be introduced when more observational data become available; (II) we adopt an exponential functional form for the breaker PDF by analogy with the observations of Melville & Matusov (2002) with the matching condition (3.14) used to determine any unknown coefficients. An important advantage of this approach is that bulk conservation of momentum and energy is enforced. The wind-speed-dependent breaker PDF used here is thus

$$P(c) \;=\; b_1 \exp(-b_2\, c/u_{*a}), \tag{3.15}$$

where (b_1, b_2) are modeling constants. Our preference for using a wind speed dependence based on u_{*a} instead of U_a follows from the explicit appearance of friction velocity in (3.14) and the numerical evaluation of (3.14) discussed near (3.16). b_1 is chosen to define a unity PDF, i.e. $\int P(c)\mathrm{d}c = 1$, while b_2 is introduced so as to satisfy the expression given by (3.14).

As noted above, measurements of the distribution of breakers and their dynamical importance are incomplete at low values of c (i.e. at small scales). The theoretical model of Phillips (1985, p. 524) predicts that the total momentum flux from wave breaking depends on the high wavenumbers at the upper end of the equilibrium range k_1. In this theory, momentum conservation requires the equilibrium range to terminate at a cutoff wavenumber $k_1 = rg/u_{*a}^2$ or minimum phase speed $c_1/u_{*a} = 1/\sqrt{r}$ with

https://doi.org/10.1017/S002211200700897X Published online by Cambridge University Press

$0 < r < 1$. Phillips (1985) estimates $r^{1/2}$ lies below 0.4 but values as large as 0.7 are possible. A typical range of values for wind speed $U_a = 15\,\mathrm{m\ s^{-1}}$ is then $c_1 \approx 0.8{-}1.5\,\mathrm{m\ s^{-1}}$. Belcher & Vassilicos (1997) and Hara & Belcher (2002) offer improvements to the model of Phillips (1985) by including the sheltering effect of long waves on short waves in the equilibrium range. The model accounts for the momentum flux from the wind to the longer waves leaving a smaller stress to force growth of the shorter waves. Assuming that the dissipation spectrum is proportional to the wind input, their model then predicts that breaking crests of shorter waves are less frequent especially in high winds $u_{*a} > 0.5\,\mathrm{m\ s^{-1}}$. An analysis of measured wave height spectra by Donelan (2001) also shows the growth of small waves is modulated by long waves leading to a net reduction in their energy density, also implying a reduced contribution to fluxes from small scale breaking. (However, the full problem of long-wave–short-wave interaction, both through direct hydrodynamic interactions and indirectly through coupling with the wind, remains one of the unsolved problems in air–sea interaction and ocean remote sensing.)

Based on these theoretical predictions and sparse observations we need to limit the breaking at small scales. However, given the uncertain nature of the available results, we simply choose to truncate the PDF of breaking at a small phase speed c_1 according to Phillips (1985) that depends on wind stress. Then (3.14) reduces to the computational rule,

$$\int_{c_1}^{c_p} |\mathscr{M}(c)|[g_t - c/u_{*a}]\, P(c)\,\mathrm{d}c = 0, \tag{3.16}$$

with the PDF given by (3.15). The PDF of breaking depends on our model for breaker momentum flux, wave age contained in the Terray parameter $g_t = g_t(c_p/u_{*a})$ and wind stress. Because of the exponential decay of the PDF at large c the integral converges rapidly and is only weakly dependent on the upper limit of integration c_p. A rapid decay of the PDF with increasing c is required in order to satisfy (3.16) since the breaker momentum $\mathscr{M}(c) \sim c^7$. This makes the determination of b_2 delicate. Based on a numerical evaluation of (3.16) we find for a given wave age c_p/u_{*a} (or Terray parameter g_t) that a single value of the modeling constant b_2 is capable of satisfying (3.16) to a good approximation across a wide range of wind speeds (5–30 m s^{-1}). This result supports our choice of wind speed scaling based on u_{*a} in (3.15).

Once the PDF of breaking is determined we retrace our steps and next find the number of breakers or breaker generation rate $\dot{N}$ by evaluating the momentum conservation rule (3.6); its right-hand side is given by (3.4). Specifically, $\dot{N}$ is chosen to satisfy

$$\boldsymbol{\tau}_a = \dot{N}\,\rho_o \int_{c_1}^{c_p}\int_0^{T(c)}\int_0^{V(c)} P(c)\,\mathscr{A}(\boldsymbol{x}, t, c)\,\mathrm{d}\boldsymbol{x}\,\mathrm{d}t\,\mathrm{d}c \tag{3.17}$$

for each wind speed and wave age. Typical PDFs and breaker generation rates are shown in figures 1 and 2 for varying U_a and c_p/u_{*a}. Notice how the PDF in figure 1 shifts towards larger scales, larger values of c, with increasing winds. Also, for a fixed wind speed larger breakers are obtained for wave ages in the intermediate range $c_p/u_* \approx 19{-}30$ (developing seas) compared to those in the equilibrium range $c_p/u_{*a} > 30$ (fully-developed seas). A similar dependence of the breaking PDF on wave age is also found in the observations of Gemmrich (2005, figure 3). The breaker generation rate decays as the wind speed increases or wave age decreases, a consequence of an overall shift in the PDF towards large-scale breaking. An important

https://doi.org/10.1017/S002211200700897X Published online by Cambridge University Press

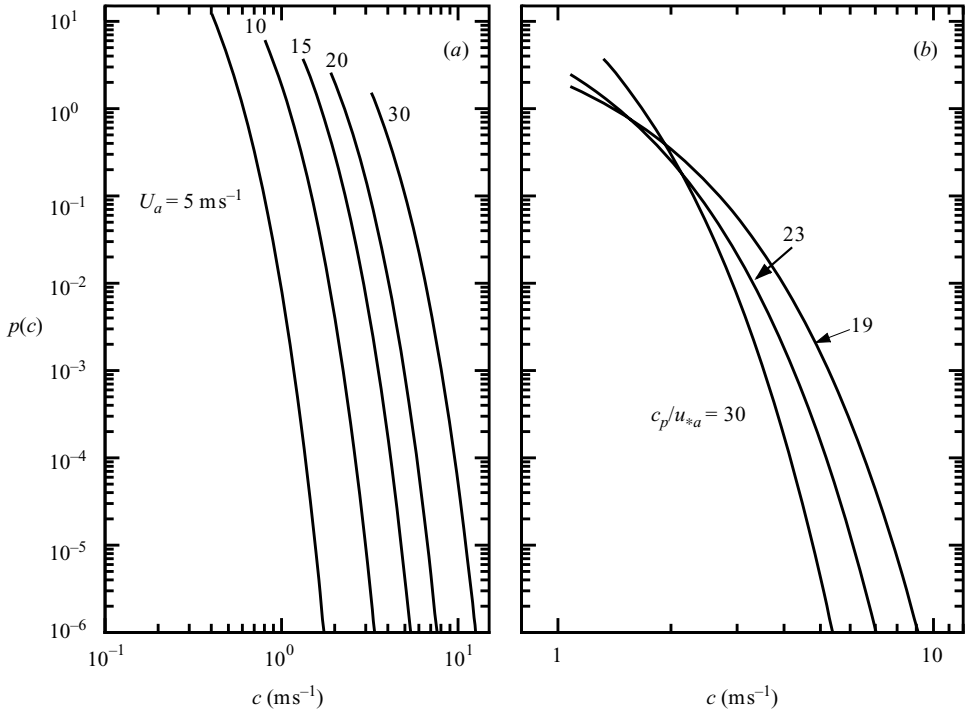


FIGURE 1. The PDF of breaking $P(c) = \mathrm{e}^{-b_2 c/u_{*a}}$ for varying wind speeds and small variations in wave age. In (*a*) $P(c)$ is shown for wind speeds $U_a = (5, 10, 15, 20, 30)$ m s^{-1} for waves approaching equilibrium $c_p/u_{*a} = 30$, Phillips parameter $r = 0.2$, and PDF constant $b_2 = 2.196$. In (*b*) the winds are held constant $U_a = 15$ m s^{-1} and the wave age varies, $c_p/u_{*a} = (30, 23, 19)$ while $b_2 = (2.196, 1.46, 1.06)$.

attribute of the exponential PDF is that it leads to rapid convergence of the integrals (3.4) and (3.8) for total breaker momentum and energy as the phase speed c increases. Computationally, this means that a finite number of draws from the PDF will closely satisfy the momentum and energy flux balances between the atmosphere and ocean. Then the details of the large-c tail of the PDF are not critical. We find more than 98% of the breaker momentum and energy is captured by breakers satisfying the criterion $P(c) > 10^{-6}$. Other functional forms for the breaker PDF do not satisfy this criterion (see Sullivan, McWilliams & Melville 2005).

The density distributions,

$$\dot{N}\,\frac{\boldsymbol{\mathcal{M}}(c,\Theta)\,c\,\mathscr{P}(c,\Theta)}{\boldsymbol{\tau}_a} \quad \text{and} \quad \dot{N}\,\frac{\boldsymbol{c}\cdot\boldsymbol{\mathcal{M}}(c,\Theta)\,c\,\mathscr{P}(c,\Theta)}{\mathcal{E}_a}, \tag{3.18}$$

provide information about the partitioning of breaker momentum and breaker energy across the range of phase speeds, c. These density distributions (or breaker spectra) are normalized so that their integrals over (c, θ) equal unity and are the companions to the wave-height spectra given by (2.1). Figure 3 shows the phase speeds (c_τ, c_E), where (3.18) attain their maximum values for varying wind speed and wave age. Notice when $c_p/u_{*a} \leqslant 30$ (or $g_t > 4$), the breaker momentum and energy distributions peak at an intermediate phase speed. For example, with $U_a = 15$ m s^{-1} and $c_p/u_{*a} = 23$ the maximum contributions to breaker momentum and energy, weighted by the PDF, occurs in the range $c \approx 3$–4 m s^{-1}. Then the lower limit c_1 plays a minor role in

https://doi.org/10.1017/S002211200700897X Published online by Cambridge University Press

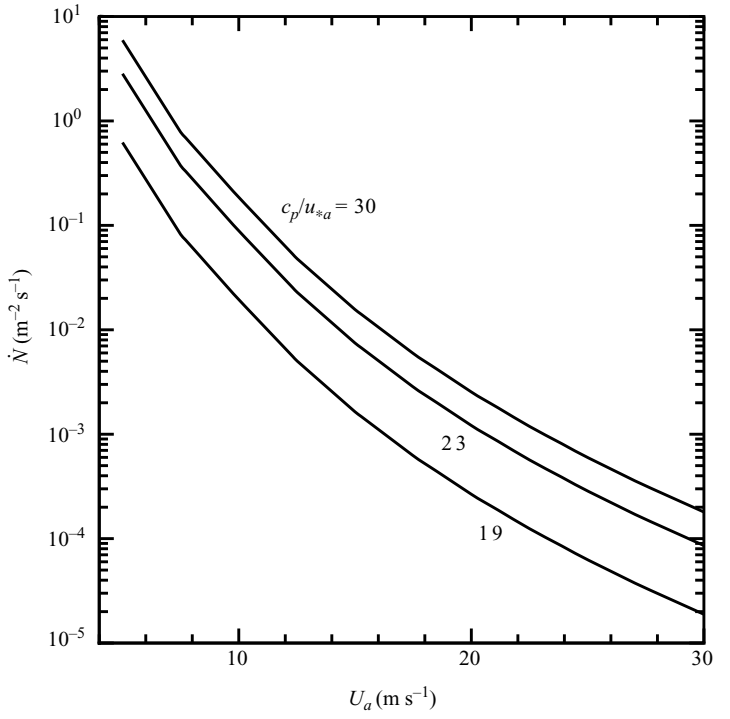


FIGURE 2. The rate of breaker generation, $\dot{N}$, for varying winds and wave age. For $(U_a, c_p/u_{*a})$ =(15 m s^{-1}, 30) and an x–y spatial domain of 300 m × 300 m approximately 5×10^6 breakers are generated per hour.

determining the PDF; the breaker PDF is more dependent on wave age and wind speed than on the minimum phase speed c_1. Melville & Matusov (2002) also found the moments $c^4\Lambda(c)$ and $c^5\Lambda(c)$ reach a maximum in a similar range of phase speeds. They estimate the wave age of their observations to be in the range $c_p/u_{*a} = 16{-}24$, which corresponds to $g_t = 8{-}5$.

The stochastic breaking model described above can be used to make an estimate of the fractional area of water covered by breakers, i.e. the whitecap coverage $\mathscr{W}_c$, which is a quantity obtained from video imagery. Field observations of visible whitecaps, i.e. those with $\lambda \geqslant 1$ m report $\mathscr{W}_c \sim 1.75\, U_a^{3.75}$ over the wind speed range $U_a = 2, 20$ m s^{-1} (Wu 1983). At higher wind speeds, closer to hurricane conditions, the available data are limited but the whitecap coverage is expected to reach a limiting value. Predictions from the rectilinear breaking model described and the breaker PDF shown in figure 1 with a lower bound $c \geqslant 1.25$ m s^{-1} (or $\lambda = 1$ m) are in good agreement with this empirical correlation, but saturate at a wind speed near $U_a \sim 17$ m s^{-1}. This agreement shows the Froude scaling used to build the discrete breaker model holds over a wide range of wind speed.

The dependence of $P(c)$ and $\dot{N}$ on wind speed and wave age, shown in figures 1 and 2, has important implications for the interactions between vortex force and breaking as discussed in § 6. For a given wind speed, growing seas are forced more strongly by the winds, the waves are generally steeper and hence break at larger scales closer to the peak in the wave spectrum. Because breaker momentum increases as c^7 the total number of breakers required to balance the wind stress decreases with decreasing

https://doi.org/10.1017/S002211200700897X Published online by Cambridge University Press

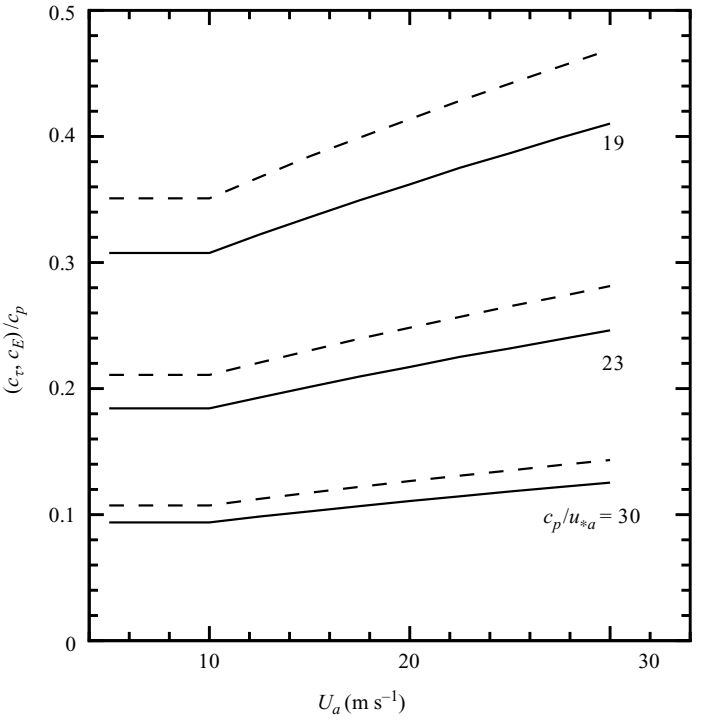


FIGURE 3. Variation of the peak phase speed for breaker momentum flux c_τ (solid line) and energy flux c_E (dashed line) with wind speed and wave age. The phase speeds are normalized by the maximum phase speed in the wave-height spectrum c_p.

wave age. Meanwhile as winds and waves approach equilibrium the overall steepness of the wave field relaxes and then breaking shifts towards the smaller (steeper) waves. Again because of the c^7 dependence the total number of breakers required to support the wind stress in the equilibrium range must then increase, i.e. many small breakers dump their momentum into currents. Larger breakers are more intermittent but their associated vorticity fields are more vigorous and capable of interacting with the vortex force. The interaction between breaking and vortex force thus exhibits a wave age dependence.

4. LES model of the OBL with wave effects

The LES model we use to examine OBL turbulence is a conventional one (Moeng 1984; Sullivan, McWilliams & Moeng 1996; McWilliams *et al.* 1997) but is extensively modified to account for surface wave effects: it is based on the incompressible Boussinesq equations with a single-point second-moment turbulent kinetic energy (TKE) closure subgrid-scale parameterization and a flat top (ocean) surface. The added wave effects are the vortex force and Lagrangian mean advection associated with Stokes drift, $\boldsymbol{u}^{St}$, and a wave-averaged increment to the pressure that arises through conservative wave–current interaction (McWilliams *et al.* 1997), as well as additional acceleration and energy generation due to non-conservative wave breaking (Sullivan *et al.* 2004). The governing equations for momentum, subgrid-scale TKE,

https://doi.org/10.1017/S002211200700897X Published online by Cambridge University Press

and density (i.e. the same as for any material scalar concentration) are the following:

$$\frac{\partial \overline{u}_i}{\partial t} = -\frac{\partial}{\partial x_j}(\overline{u}_j\overline{u}_i + \tau_{ij}) - \delta_{i3}\frac{g\overline{\rho}}{\rho_o} - \frac{\partial \pi}{\partial x_i} - \epsilon_{ijk}f_j\left(\overline{u}_k + u_k^{St}\right) + \epsilon_{ijk}u_j^{St}\overline{\omega}_k + \sum_m \overline{A}_i^m, \tag{4.1a}$$

$$\frac{\partial e}{\partial t} = \cdots - u_j^{St}\frac{\partial e}{\partial x_j} - \tau_{ij}\frac{\partial u_i^{St}}{\partial x_j} + \sum_m W^m, \tag{4.1b}$$

$$\frac{\partial \overline{\rho}}{\partial t} = -\frac{\partial}{\partial x_j}(\overline{u}_j\overline{\rho} + \tau_{j\rho}) - u_j^{St}\frac{\partial \overline{\rho}}{\partial x_j}. \tag{4.1c}$$

In (4.1) spatially filtered (or resolved) variables are denoted with an overbar. Here ($\overline{\boldsymbol{u}}$, $\overline{\omega} = \nabla\times\overline{\boldsymbol{u}}$) are the resolved-scale velocity and vorticity; e is the subgrid-scale TKE; $\overline{\rho}$ is the density; and the generalized pressure field is

$$\pi = \frac{\overline{p}}{\widetilde{\rho}_o} + \frac{2}{3}e + \frac{1}{2}\left[\left(\overline{u}_i + u_i^{St}\right)\left(\overline{u}_i + u_i^{St}\right) - \overline{u}_i\overline{u}_i\right]. \tag{4.2}$$

Note with this flux form of the momentum equations, π reduces to $\overline{p}/\rho_o + 2e/3$ in the absence of a wave field. The effects of $m = 1, \ldots, M$ discrete wave-breaking events are represented by a resolved-scale acceleration, $\overline{\boldsymbol{A}}^m$, and a subgrid-scale TKE generation rate, W^m. The dots in the TKE equation denote all the other terms (namely advection, production, buoyancy, diffusion and dissipation) that appear in the conventional closure formulation. Other variables appearing in this equation set are: the Coriolis frequency, $\boldsymbol{f} = (0, 0, f)$; reference density, $\widetilde{\rho_o}$; gravitational acceleration, g; and subgrid-scale momentum and density fluxes, $(\tau_{ij}, \tau_{i\rho})$, respectively. These subgrid-scale fluxes are modeled using the eddy viscosity prescription described by Moeng (e.g. Moeng 1984) and Sullivan *et al.* (1994) which implies that the principal feedback of e on $\overline{\boldsymbol{u}}$ and $\overline{\rho}$ occurs through subgrid-scale mixing with eddy viscosity and diffusivities $(\nu_t, \nu_s) \propto e^{1/2}$.

This LES model (4.1) includes some wave effects without actually resolving the oscillatory and breaking wave motions themselves. By otherwise neglecting wave dynamics, there is an implicit assumption that the wave quantities are unaffected by the currents; this is explicit in the particular rules specified for $\overline{\boldsymbol{A}}$, W and $\boldsymbol{u}^{St}$. Further simplifications are the neglect of the positive buoyancy caused by air entrained into bubbles in breaking waves (Lamarre & Melville 1991) and the assumption of a linearized equation of state where density is proportional to temperature θ. Since the wave influences on deforming the oceanic free surface are averaged out in this formulation, the wave effects on pressure do not enter explicitly into the model since π is calculated by solving the pressure-Poisson equation derived from taking the divergence of the momentum equation and applying the incompressibility condition. This is the standard method of determining the pressure with numerical techniques based on fractional step methods (Armfield & Street 1999; Ferziger & Perić 2002).

4.1. *Vortex force*

Wave-averaged influences enter as Stokes advection in the TKE and scalar equations and as a generalized vortex force, $\boldsymbol{u}^{St}\times(f\hat{\boldsymbol{z}}+\overline{\boldsymbol{\omega}})$, in the momentum equation. The vortex force has a significant influence on the turbulent eddies and their vertical fluxes in the OBL through the generation of Langmuir circulations (Craik & Leibovich 1976; McWilliams *et al.* 1997). Wave effects also directly impact subgrid-scale energy since its balance equation includes a Stokes production term, i.e. subgrid-scale stresses

https://doi.org/10.1017/S002211200700897X Published online by Cambridge University Press

working on the vertical gradient of the Stokes drift. An analogous term appears in the TKE balance for resolved scales (McWilliams *et al.* 1997, equation 5.1), and Stokes production has recently been included in some one-dimensional, Reynolds-averaged models of the OBL, (Kantha & Clayson 2004). In contrast to the Reynolds-averaged models, the local subgrid-scale energy transfer from Stokes production in an LES can be either positive or negative since $\partial u^{St}/\partial z$ has a given orientation and sign and τ_{13} fluctuates in time and space over the LES grid. Because of the eddy-viscosity closure for vertical momentum flux, the long-time impact of Stokes production for e depends on the current and Stokes drift shears; i.e. for a steady uniform $\boldsymbol{u}^{St}$,

$$-\left\langle \tau_{ij}\frac{\partial u_i^{St}}{\partial x_j}\right\rangle = \left\langle \nu_t\left(\frac{\partial \overline{u}}{\partial z}+\frac{\partial \overline{w}}{\partial x}\right)\right\rangle \frac{\partial u^{St}}{\partial z}+\left\langle \nu_t\left(\frac{\partial \overline{v}}{\partial z}+\frac{\partial \overline{w}}{\partial y}\right)\right\rangle \frac{\partial v^{St}}{\partial z}, \tag{4.3}$$

where $\langle\ \rangle$ indicates an ensemble average. The magnitude of the Stokes drift often exceeds the horizontal current speed near the surface, leading to substantial TKE advection. Finally, the coupling of u^{St} and e is implicit because of the influence of waves on the resolved currents. Stokes advection and production of subgrid-scale e, which are absent in our previous LES (McWilliams *et al.* 1997), are expected to be more important in the current simulations that account for a full wave spectrum.

4.2. *Resolved and subgrid-scale breakers*

In order to implement our LES with breakers we need to account for the spatial filtering associated with numerical discretization. Formally, a filtered field $f(\boldsymbol{x}) \rightarrow \overline{f}(\boldsymbol{x})$ is defined by the operation,

$$\overline{f}(\boldsymbol{x}) = \int f(\boldsymbol{x}')\, G(\boldsymbol{x}-\boldsymbol{x}')\, \mathrm{d}\boldsymbol{x}', \tag{4.4}$$

where $G(\boldsymbol{x})$ is a low-pass spatial filter with characteristic length scale Δ; resolved and subgrid-scale motions have scales $l > \Delta$ and $l < \Delta$, respectively.

The computational grid spacing limits our ability to temporally and spatially resolve the breaker wave field. Thus we introduce a minimum breaker phase speed $c_\Delta = (g\Delta/2\pi)^{1/2}$, based on the LES filter scale Δ, to separate resolved and unresolved breakers. The intermittent space-time properties of breakers $c < c_\Delta$ cannot be captured on the LES grid, but their bulk influence must still be accounted for as they contribute to the overall fluxes of momentum and energy. A consistent scale decomposition of the momentum flux due to breaking is then

$$\boldsymbol{\tau}_a = \dot{N}\int_0^{c_\Delta} \boldsymbol{\mathcal{M}}(c)\, P(c)\, \mathrm{d}c + \dot{N}\int_{c_\Delta}^{c_p} \boldsymbol{\mathcal{M}}(c)\, P(c)\, \mathrm{d}c, \tag{4.5}$$

where the first and second terms on the right-hand-side are contributions from subgrid-scale and resolved breakers, respectively. Equation (4.5) follows from combining (3.4), (3.6) and (3.7) and the discussion in § 3.3. In computational practice, any draws made from the PDF with phase speed $c < c_\Delta$ are considered subgrid-scale and parameterized as a constant (viscous) stress $\boldsymbol{\tau}_o$ applied at the water surface. Thus the LES representation of (4.5) is

$$\boldsymbol{\tau}_a = \boldsymbol{\tau}_o + \dot{N}\int_{c_\Delta}^{c_p} \boldsymbol{\mathcal{M}}(c)\, P(c)\, \mathrm{d}c. \tag{4.6}$$

The subgrid-scale contribution to momentum flux $\boldsymbol{\tau}_o$ is known when the grid mesh is specified, i.e. $\boldsymbol{\tau}_o$ is calculated prior to integration of the governing equations. Note (4.5) behaves properly with changing grid spacing. In the limit where Δ is large all

https://doi.org/10.1017/S0022112007008977X Published online by Cambridge University Press

breaking becomes subgrid-scale and then the surface forcing reduces to conventional constant stress.

By analogy with momentum flux the decomposition of the wave (breaker) energy flux into small- and large-scale pieces is

$$\mathcal{E}_a \;=\; \mathcal{E}_o \;+\; \dot{N} \int_{c_\Delta}^{c_p} \boldsymbol{c}\cdot\boldsymbol{\mathcal{M}}(c)\, P(c)\, \mathrm{d}c\,, \tag{4.7}$$

where

$$\mathcal{E}_o \;=\; \dot{N} \int_{0}^{c_\Delta} \boldsymbol{c}\cdot\boldsymbol{\mathcal{M}}(c)\, P(c)\, \mathrm{d}c\,. \tag{4.8}$$

The energy flux $\mathcal{E}_o$ from small-scale breakers $c < c_\Delta$ is tightly confined to the water surface, while the energy flux from larger-scale breakers $c > c_\Delta$ is naturally distributed over a finite horizontal extent and vertical depth spanning multiple gridpoints.

In order to expose the breaker energetics in our LES model we construct kinetic energy equations for the total, resolved and subgrid-scale components. The contribution of breakers to the evolution of filtered total kinetic energy per unit of water mass $\overline{E} = \overline{u_i\, u_i}/2$,

$$\frac{\partial \overline{E}}{\partial t} \;\equiv\; \overline{u_i\, \frac{\partial u_i}{\partial t}} \;= \cdots + \overline{u_i\, A_i}\,, \tag{4.9}$$

depends on the (unknown) correlation between total velocity and breaker impulses. Here dots denote all other terms in the kinetic energy equation, i.e. advection, production, buoyancy, diffusion and dissipation (Moeng 1984). Combining (4.9) with the transport equation for resolved kinetic energy $E_r = \overline{u_i}\,\overline{u_i}/2$,

$$\frac{\partial E_r}{\partial t} \;\equiv\; \overline{u_i}\, \frac{\partial \overline{u_i}}{\partial t} \;= \cdots + \overline{u_i}\,\overline{A_i}\,, \tag{4.10}$$

leads to the TKE equation for subgrid-scale energy $e = (\overline{u_i\, u_i} - \overline{u_i}\,\overline{u_i})/2$

$$\frac{\partial e}{\partial t} = \frac{\partial \overline{E}}{\partial t} \;- \frac{\partial E_r}{\partial t} \;= \cdots + W\,. \tag{4.11}$$

In (4.11), the subgrid-scale work done by breaking,

$$W \;=\; \overline{u_i\, A_i} \;-\; \overline{u_i}\,\overline{A_i}\,, \tag{4.12}$$

is unknown and must be modeled consistently in terms of the resolved field to match the input energy flux $\mathcal{E}_a$. Equating the volume work done by breakers in the water column to the input energy flux from winds to waves requires

$$\frac{\mathcal{E}_a}{\rho_o} = \frac{1}{\mathcal{S}} \int_{\mathcal{V}} \overline{u_i\, A_i}\, \mathrm{d}\mathcal{V} \;=\; \frac{1}{\mathcal{S}} \int_{\mathcal{V}} \left(\overline{u_i}\,\overline{A_i} \;+\; W\right) \mathrm{d}\mathcal{V}\,. \tag{4.13}$$

Inspection of (4.13), (4.7), and (4.8) guides our model design for W. We adopt the two-part model,

$$W(\boldsymbol{x}, t) \;= \frac{1}{\rho_o}\, \frac{\partial \mathcal{E}_o}{\partial z} H(z) \;+\; \sum_m k_w\, \boldsymbol{c}^m \cdot \boldsymbol{A}^m\,, \tag{4.14}$$

where the Heaviside function is defined as $H(z \geqslant 0) = 1$, $H(z < 0) = 0$. The first term in (4.14) is the gradient of the small-scale energy flux from the wave field at the water surface ($z = 0$) and can be explicitly computed from the discrete event breaker model and the PDF of breaking; it varies with wind speed, wave age and LES filter scale Δ. The second term in (4.14) is the work done by the sum of m individual large-scale

https://doi.org/10.1017/S002211200700897X Published online by Cambridge University Press

breakers with $c > c_\Delta$; it distributes breaker work over a finite depth and mimics the intermittent space-time character of the momentum impulses. In principle, given $\mathscr{E}_a$ and $\mathcal{E}_o$ the work constant k_w is chosen to satisfy (4.13). However, because of the dependence on the resolved field in (4.13), k_w can only be found iteratively, i.e. by first choosing a trial k_w, running the LES code, and post-checking the results against $\mathscr{E}_a$. Then k_w is adjusted accordingly to satisfy (4.13); we find $k_w \sim 1.3$.

It is interesting to compare our model for breaker work (4.14) with the breaker energy flux model first proposed by Craig & Banner (1994) (the latter is used in the LES described by Noh *et al.* (2004)). Craig & Banner (1994) collapse the influence of breaking onto the water surface, with no depth dependence, and replace the temporal and spatial variability of breaking by an ensemble average inherent in second-order closure modeling. The first term of (4.14) is similar to the Craig & Banner (1994) model but only has contributions from the subgrid-scale piece of the wave spectrum, i.e. breakers with $c < c_\Delta$. This is consistent with the LES decomposition into resolved and subgrid-scale fields. For a fixed wave state, as $\Delta \to \infty$ the work done by breaking tends to the ensemble average. Unlike Craig & Banner (1994) $\mathcal{E}_o$ varies with wave age because of the dependence of the PDF on wave state.

5. Simulations with wave effects

In order to evaluate the impacts and interactions between wave breaking, vortex force and turbulence we incorporated the modeling ideas and equations of § 2-4 into a large-eddy simulation code for the OBL. Similarly to McWilliams *et al.* (1997) the boundary conditions are periodic in the lateral $(x-y)$ directions, no flow at the lower boundary with a radiation condition allowing gravity waves to escape (Klemp & Durran 1983; McWilliams *et al.* 1997). The imposed surface stress depends on wind speed and the PDF of breaking as discussed previously. The LES algorithm with stochastic breakers is sufficiently novel (and complex) that a brief description of the code is provided in the Appendix. Further algorithmic details, numerical method and the subgrid-scale model used to solve the equation set (without wave breaking) are fully presented in McWilliams *et al.* (1997), Sullivan *et al.* (1996), Sullivan, McWilliams & Moeng (1994) and Moeng (1984). A direct numerical simulation code for the OBL with single-scale breakers is outlined in Sullivan *et al.* (2004).

An exhaustive exploration of the large parameter space encompassing variations in wind speed, wave age, buoyancy, varying combinations of wave effects and other physical processes is not possible because of finite computational resources. The scope of the current study focuses on OBL dynamics when wave influences are important and in particular when intermittent breaking is a dominant surface-layer process. For the present investigation we choose a moderately high wind speed $U_a = 15$ m s^{-1}. The suite of experiments compares four types of simulations: a baseline simulation driven by uniform (constant) surface stress with no wave effects; the conventional posing plus wave-averaged Stokes drift terms (McWilliams *et al.* 1997); a posing with stochastic forcing representing breaking waves; and, a posing with stochastic forcing plus Stokes drift terms. In addition, solution sensitivity tests are performed to examine the consequences of modestly varying wave age (as contained in the Terray parameter), an increase in wind speed to $U_a = 30$ m s^{-1} and a decrease in the Stokes drift profile for a fetch-limited wave spectrum. These explorations are intended to illustrate the solution robustness and are mild excursions into the regime of disequilibrium winds and waves. A summary of the simulations and the naming conventions used to identify the various cases is given in table 1. A wave age range is

https://doi.org/10.1017/S002211200700897X Published online by Cambridge University Press

Run name	Forcing	Stokes drift	c_p/u_{*a}	g_t	U_a (m s^{-1})	u_{*o} (m s^{-1})	h (m)
U	uniform stress no wave effects	NA	NA	NA	15	0.0187	−48.6
$U + St$	uniform stress	Yes	NA	NA	15	0.0187	−51.3
$B1$	breaking	No	>30	3.9	15	0.0187	−46.6
$B1 + St$	breaking	Yes	>30	3.9	15	0.0185	−48.6
$B2$	breaking	No	23 ± 3	5.5	15	0.0184	−49.4
$B2 + St$	breaking	Yes	23 ± 3	5.5	15	0.0187	−46.3
$B3$	breaking	No	19 ± 3	7.4	15	0.0187	−52.1
$B3 + St$	breaking	Yes	19 ± 3	7.4	15	0.0195	−48.4
†$B3 + FSt$	breaking	Yes	19 ± 3	7.4	15	0.0194	−46.7
$H1 + St$	breaking	Yes	>30	3.9	30	0.0451	−71.7

TABLE 1. Simulation properties

† The Stokes drift in this simulation is based on a fetch-limited wave-height spectrum as discussed in § 7.

supplied in table 1 to indicate the uncertainty in the estimate of g_t based on the data of Terray *et al.* (1996, figure 8).

The setup of the simulations is similar to McWilliams *et al.* (1997) except we use larger domains and finer grid resolutions. The initial state of the OBL is neutral stratification from the surface to a mixed layer depth $h = -32$ m. Below $z < h$ the thermocline is stably stratified at a rate of 0.05 K m^{-1}. In order to examine scalar mixing a small heat flux $Q_* = 5 \times 10^{-7}$ K m s^{-1} is imposed at the surface. In all simulations the Coriolis parameter $f = 10^{-4}$ s^{-1}. For the wind speed $U_a = 15$ m s^{-1} and assuming a density ratio $\rho_o/\rho_a = 10^3$ the atmosphere and ocean friction velocities are $u_{*a} = 0.591$ m s^{-1} and $u_{*o} = 0.0187$ m s^{-1}, respectively. The computational domain $(L_x, L_y, L_z) = (300, 300, -110)$ m is discretized with (300, 300, 128) gridpoints (horizontal grid spacing $\Delta x = \Delta y = 1.0$ m). At the higher wind speed $U_a = 30$ m s^{-1}, a larger domain is used, (750, 750, −170) m, and is discretized with (500, 500, 128) gridpoints ($\Delta x = \Delta y = 1.5$ m). In this case the rate of stable stratification below the initial thermocline depth is doubled 0.10 K m^{-1}. Vertical meshes are generated using constant algebraic stretching, i.e. with the ratio of any two vertical cells $K = \Delta z_{k+1}/\Delta z_k$ held constant. Stretching factors $K < 1.012$ yield flexible meshes capable of concentrating the grid near the surface, but extending deep into the water. This small value of K ensures that the mesh varies smoothly in the vertical direction. Thus the ratio of horizontal and vertical spacing at the first z-level below the water surface $\Delta x/\Delta z_1 < 2.6$. LES with this horizontal–vertical mesh ratio yields good simulations of atmospheric convection (Moeng & Wyngaard 1989) and this mesh ratio is well within the acceptable limits suggested by Scotti, Meneveau & Lilly (1993). The influence of the subgrid-scale (SGS) motions is not significant as the SGS fluxes are small over the entire computational domain, especially in simulations with wave breaking. To arrive at a (statistical) steady state all simulations are run for more than 30 large eddy turnover times $T_e = -h/u_{*o}$ or more than 25 physical hours requiring [90 000 − 240 000] computational steps. As is customary practice, statistics are generated by combining spatial $x-y$ and temporal averaging; these averages are indicated by $\langle\ \rangle$. The mixed-layer depth is a function of time and also varies with spatial position. At any t, we deduce an estimate of the mean mixed-layer depth h using the maximum scalar gradient method described by Sullivan *et al.* (1998). This

https://doi.org/10.1017/S002211200700897X Published online by Cambridge University Press

method is able to track the average movement of the turbulent layer and provides a good estimate of the average entrainment velocity across the thermocline.

With wave effects the vertical profile of the Stokes drift is numerically evaluated for a full wave spectrum as described in § 2.1. Based on the Stokes profile at a depth $z = 1$ m, the turbulent Langmuir number $La_t = \sqrt{u_{*o}/u^{St}} \approx 0.3$, and thus wave–current interactions are important (McWilliams *et al.* 1997) in the chosen wind-speed regime. The partitioning of the atmospheric momentum flux (2.5) into resolved and subgrid breaker pieces depends on the grid resolution, wind speed and the breaker PDF as discussed in §§ 3.3 and 4.2. For the grid resolution used, winds $U_a = 15$ m s^{-1}, and near equilibrium winds and waves $g_t \approx 3.9$, the ratio of the subgrid-scale uniform stress to the total wind stress $|\boldsymbol{\tau}_o|/|\boldsymbol{\tau}_a| \approx 0.1$. For higher wind speeds and larger values of g_t this ratio rapidly decreases to values less than 1%. Hence for the majority of the simulations intermittent breaking is responsible for transmitting 90–100% of the atmospheric stress to the water column and is the main mechanism for mean current generation in the simulations. Below a depth $z < -4$ m the SGS contribution to the momentum fluxes is less than 2% of the surface stress u_{*o}^2.

6. Results

The observed response of the OBL to the vortex force and wave breaking suggests a connection between the surface wave conditions and vertical mixing in the OBL. We find that the mean currents, turbulence variances (and TKE), turbulence dissipation, scalar and momentum fluxes and entrainment at the thermocline all exhibit varying degrees of sensitivity to the surface wave field. In general, simulations with explicit wave influences differ from their counterparts driven by constant stress and no wave effects. An important parameter is the PDF of breaking and its dependence on wave state. For a given wind speed $P(c)$ shifts towards larger-scale breaking as wave age c_p/u_{*a} decreases from 30 to 19. At the same time the number of breakers in the computational domain decreases, consistent with the need to obey momentum and energy conservation. The shift towards larger-scale breaking promotes interactions between breaking turbulence and vortex force.

6.1. *Mean current and momentum-flux profiles*

In order to examine the momentum balance in the presence of waves we form the ensemble-average integral momentum budget from the LES equations (4.1*a*). For the conditions of the simulations, i.e. horizontally homogeneous flow, no flow as $z \to -\infty$, aligned surface winds and waves with $\boldsymbol{u}^{St} = [u^{St}(z), 0, 0]$, the momentum budget for statistically steady flow is

$$\langle \overline{u}\,\overline{w} \rangle + \langle \tau_{13} \rangle - \int_{-\infty}^{z} \langle \overline{A} \rangle \, \mathrm{d}z = f \int_{-\infty}^{z} \langle \overline{v} \rangle \, \mathrm{d}z \tag{6.1a}$$

$$\langle \overline{v}\,\overline{w} \rangle + \langle \tau_{23} \rangle = -f \int_{-\infty}^{z} \langle \overline{u} + u^{St} \rangle \, \mathrm{d}z, \tag{6.1b}$$

where $\langle\ \rangle$ denotes an ensemble average. This expression illustrates how resolved and subgrid-scale turbulence fluxes, waves and mean currents contribute to the bulk momentum balance. It contains explicit wave influences in the form of Ekman–Stokes transport $\int u^{St} \mathrm{d}z$ (McWilliams *et al.* 1997) and a new contribution from vertically distributed breakers. Note in the y-budget equation the locally varying vortex force $u^{St}\omega_3$, which plays an important role in generating convergence lines, does not appear since $\langle u^{St}\omega_3 \rangle = 0$. The vertical profile of average breaker momentum flux $-\int \langle \overline{A} \rangle \mathrm{d}z$

https://doi.org/10.1017/S0022112007008977X Published online by Cambridge University Press

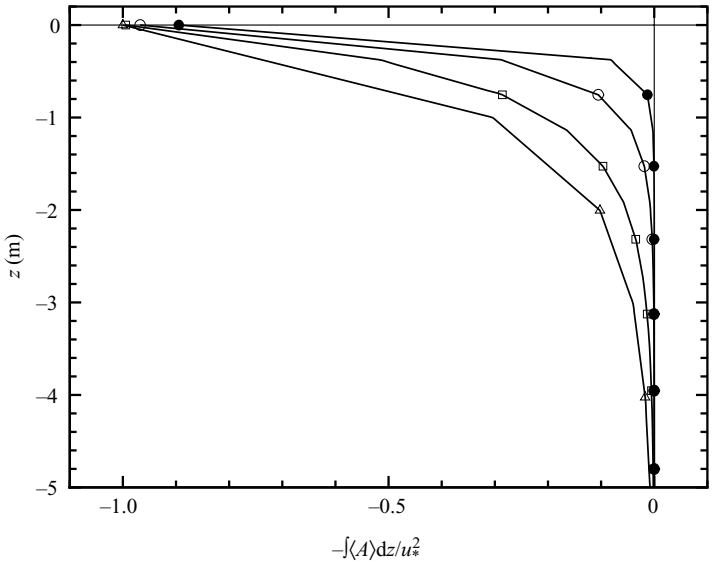


FIGURE 4. The depth variation of the ensemble-average breaker momentum flux for varying wave age and wind speed: $(U_a, c_p/u_{*a})$ =(15 m s^{-1}, 30), •; (15 m s^{-1}, 23), ○; (15 m s^{-1}, 19), □; (30 m s^{-1}, 30), △. The breaker momentum flux is normalized by the water friction velocity u_{*o}^2.

obtained from the simulations is shown in figure 4. As expected its surface value varies with wave age and wind speed, as discussed in § 3. Intermittent breakers account for more than 90% of the total momentum transport to the underlying currents for the forcing conditions and grid resolution of the simulations. The breaker momentum flux decays rapidly with z because of the exponential decay of the vertical shape function $\mathscr{Z}$ (Sullivan *et al.* 2004, (3.3*d*)) and the small value of the depth penetration constant $\chi = 0.2$; for example the breaker momentum flux with $U_a = 15\,\mathrm{m\,s^{-1}}$ and $g_t = 3.9$ becomes negligible below $z \approx -1\,\mathrm{m}$ and at higher winds, where the PDF includes larger breakers, extends down to about $z \approx -5\,\mathrm{m}$. Notice for intermediate wave age the breaker contribution at $15\,\mathrm{m\,s^{-1}}$ moves towards the variation at $30\,\mathrm{m\,s^{-1}}$ consistent with the PDF variations shown in figure 1.

In order to compare fairly average currents from different simulations, which have slightly different integration periods, the mean currents are corrected for the presence of inertial oscillations. Given the Coriolis parameter, the amplitude and phase of the inertial oscillation is determined by a least-squares curve-fitting procedure applied over the entire time period of the simulations (see Lin *et al.* 1996). The deduced low-frequency inertial oscillation is then subtracted from each current component. Vertical profiles of the mean currents, shown in figure 5, illustrate the impact of the various wave processes under conditions approaching a fully-developed sea. The most striking feature of the results is a clear grouping based on the presence or absence of Stokes drift. For wind–wave equilibrium conditions, breaking does not significantly modify the mean direction and magnitude of the average currents. This is an interesting result given the radical difference in the level of intermittent forcing between simulations with and without breaking. We emphasize that in cases $(B1, B1 + St)$ mean currents are generated solely by spatially distributed random impulses near the water surface, while in cases $(U, U + St)$ a conventional uniform surface stress boundary condition

https://doi.org/10.1017/S002211200700897X Published online by Cambridge University Press

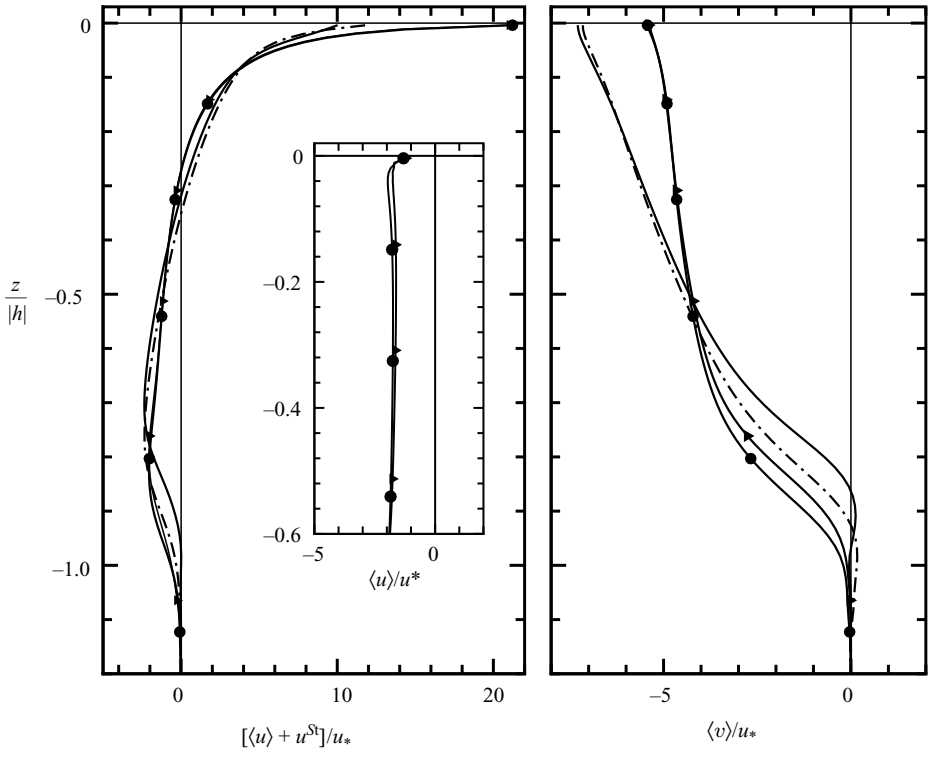


FIGURE 5. The sum of the mean current and Stokes drift profiles for simulations with: no wave effects, dash-dot line; Stokes drift only, ►; breaking only, solid line; Stokes drift plus breaking, •. The inset shows just the Eulerian mean current profile $\langle u\rangle/u_{*o}$ for simulations with Stokes drift only (►) and Stokes drift plus breaking (•). The winds and waves are near full equilibrium with $(c_p/u_{*a}, g_t) = (30, 3.9)$.

is applied at $z = 0$. Under the assumption that breaking is the main path to current generation, these results imply the cumulative effect of intermittent breaking is to generate mean currents typical of an OBL forced by constant surface stress. Closer inspection of the results shows the mean surface current obtained with breaking only (no vortex force) weakens as wave age decreases. As c_p/u_{*a} diminishes the probability of large-scale breaking increases, which induces a substantial increase in near-surface eddy viscosity ν_t accompanied by a reduction in the current shear. A similar effect was also observed in our idealized DNS (Sullivan *et al.* 2004) but is weaker in the present LES which includes a spectrum of breaking waves.

The presence of Stokes drift, however, has a dramatic impact on the mean currents and plays a dominant role even as the level of breaking increases. The present results are at least qualitatively consistent with the previous LES of McWilliams *et al.* (1997), who applied a Stokes profile based on a monochromatic wave field and drove the OBL with uniform surface stress. Potent Langmuir cells, generated by the wave field, promote efficient vertical transport leading to well-mixed (u, v)-current profiles throughout the bulk of the mixed layer with a noticeable turn to the right as $z \to h$. Langmuir cells also indirectly impact entrainment of cool water as they enhance the current shear in the region $z \approx h$.

The coherent structures generated by the vortex force increase the efficiency of the momentum transport as observed in figure 6. For a given z, the total turbulent fluxes

https://doi.org/10.1017/S002211200700897X Published online by Cambridge University Press

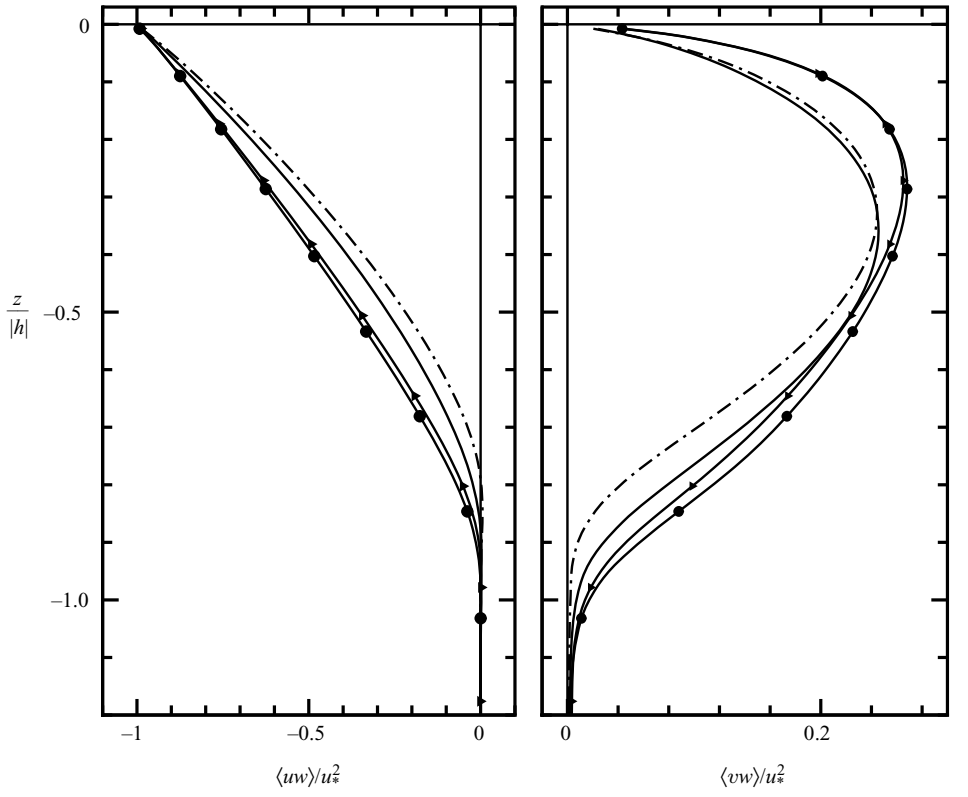


FIGURE 6. Vertical profiles of the mean total (resolved plus SGS) vertical momentum flux $\langle \overline{\boldsymbol{u}'w}\rangle$ for simulations with: no wave effects, dash-dot line; Stokes drift only, ►; breaking only, solid line; Stokes drift plus breaking, •.

$\langle \overline{u'w}\rangle$ and $\langle \overline{v'w}\rangle$ are enhanced compared to the situation with no wave influences and this enhancement is only slightly modified by the presence of significant wave breaking for fully developed waves. The profile (figure 7) of mean eddy viscosity for momentum K_m, deduced from

$$\langle \overline{\boldsymbol{u}'w}\rangle \;=\; -K_m\,\mathrm{d}\langle \overline{\boldsymbol{u}}\rangle/\mathrm{d}z\,, \tag{6.2}$$

illustrates the increased mixing efficiency generated by Langmuir cells. The enhancement compared to cases with no vortex force is primarily a reflection of the decrease in mean current shear shown in figure 5. The sign change of K_m in the interval $-0.2 < z/|h| < 0$ is a consequence of subtle slope changes in the $\langle \overline{v}\rangle$ and $\langle \overline{u}\rangle$ currents near $z/|h| \approx (-0.2, -0.05)$, respectively. Vertical oscillations in the K_m profile in the case with vortex force appear to be smoothed by the presence of stochastic breaking. The negative values of the mixing coefficient are evidence of non-local vertical transport and clearly show the inadequacy of a mean eddy viscosity assumption in the presence of Langmuir cells.

6.2. *Variance, TKE and dissipation profiles*

Inspection of the TKE and turbulence variance profiles (figures 8 and 9) highlights the competition and tradeoffs between uniform and stochastic forcing, and Stokes drift at wind speed $U_a = 15\,\mathrm{m\,s^{-1}}$. Similar to the mean current profiles, the results for the resolved variances can be grouped depending on the presence or absence of

https://doi.org/10.1017/S002211200700897X Published online by Cambridge University Press

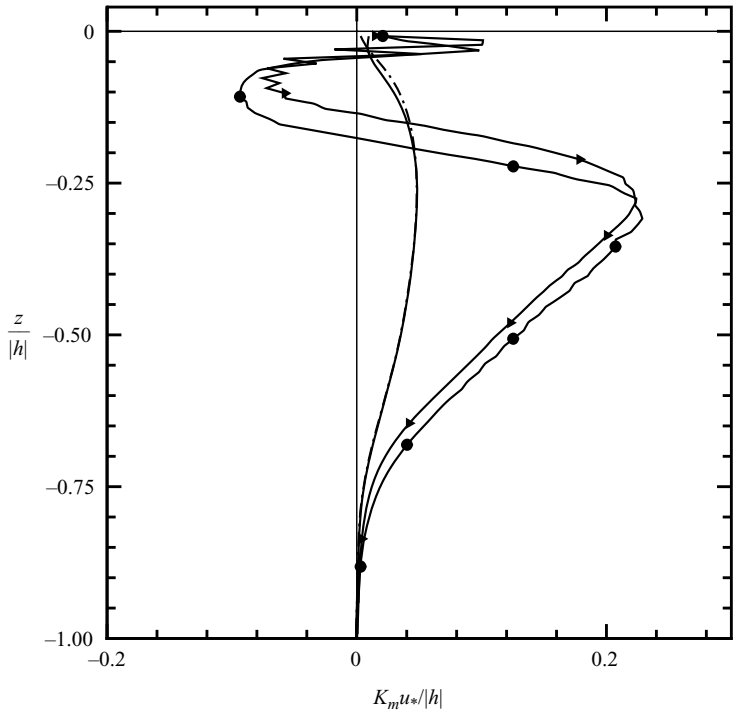


FIGURE 7. Profile of eddy viscosity for momentum $K_m = -\langle \overline{u'w} \rangle \cdot \mathrm{d}\langle \overline{u} \rangle / \mathrm{d}z \;/\; |\mathrm{d}\langle \overline{u} \rangle / \mathrm{d}z|^2$ for simulations with: no wave effects, dash-dot line; Stokes drift only, ►; breaking only, solid line; Stokes drift plus breaking, •.

vortex force. First, comparing flows driven by breaking or uniform stress (no Stokes drift), we notice that the influence of breaking is confined to the near-surface waters $-0.1 < z/|h| < 0$, a depth of 5 m or less that is expected based on the vertical distribution of breaker impulses (figure 4). In the LES, stochastic breaking lowers the u-variance similarly to the trend observed in our DNS, which had relatively large breakers of a single scale. The biggest impact of the wave field on the turbulence results from the vortex force. The near-surface reduction in the u-variance, strong enhancement of the v-variance and the significant increase in the w-variance below the water surface observed here are also present in the LES of McWilliams *et al.* (1997) obtained with a monochromatic wavefield,. These changes in the turbulence variances are attributable to the presence of organized Langmuir cells which persist in the presence of breaking. Closer inspection of runs $B1 + St$ and $U + St$ indicates a reduction in the v-variance in the presence of breaking near the water surface. This trend becomes more apparent as the dominant scale of breaking increases, i.e. for less developed waves $c_p/u_{*a} < 30$ (results not shown). The reduction in the lateral variance implies less coherent Langmuir cells; this finding is supported by the flow visualization presented later. The modulation of the strength and organization of Langmuir cells by large-scale breaking waves in the LES is an interesting result as previous LES show strong intensification and reduction in scale of the Langmuir cells as the LES grid resolution is refined (McWilliams *et al.* 1997).

Breaking and the vortex force elevate the TKE near the water surface compared to simulations without wave influences; the total (resolved plus SGS) energy normalized by u_{*o}^2 increases from 6 to more than 20 with a large percentage of the increase due to

https://doi.org/10.1017/S002211200700897X Published online by Cambridge University Press

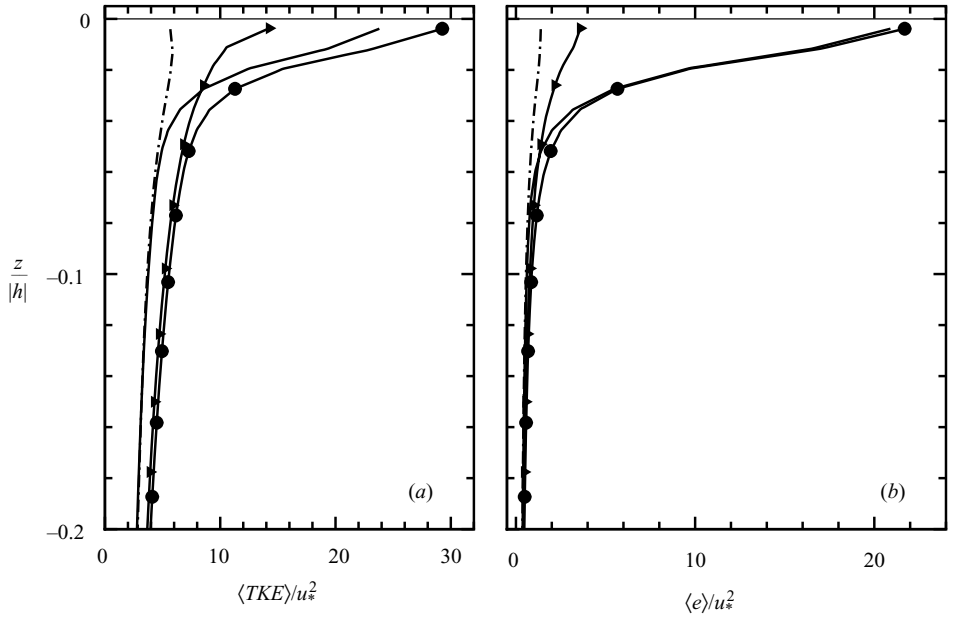


FIGURE 8. TKE profiles close to the water surface $-0.2 < z/|h| < 0$ for simulations with-no wave effects, dash-dot line; Stokes drift only, ►; breaking only, solid line; Stokes drift plus breaking, •. The wave age is $c_p/u_{*a} = 30$. Panel (*a*) total (resolved plus SGS) and (*b*) subgrid-scale energy.

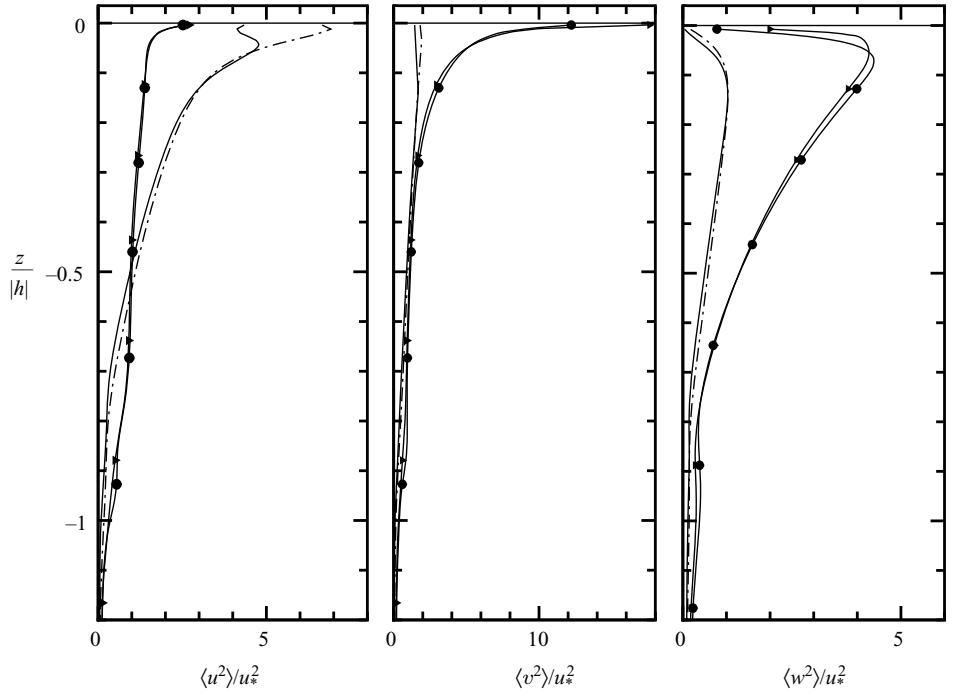


FIGURE 9. Variance profiles of the resolved velocity components for simulations with: no wave effects, dash-dot line; Stokes drift only, ►; breaking only, solid line; Stokes drift plus breaking for winds and waves near equilibrium, •.

https://doi.org/10.1017/S002211200700897X Published online by Cambridge University Press

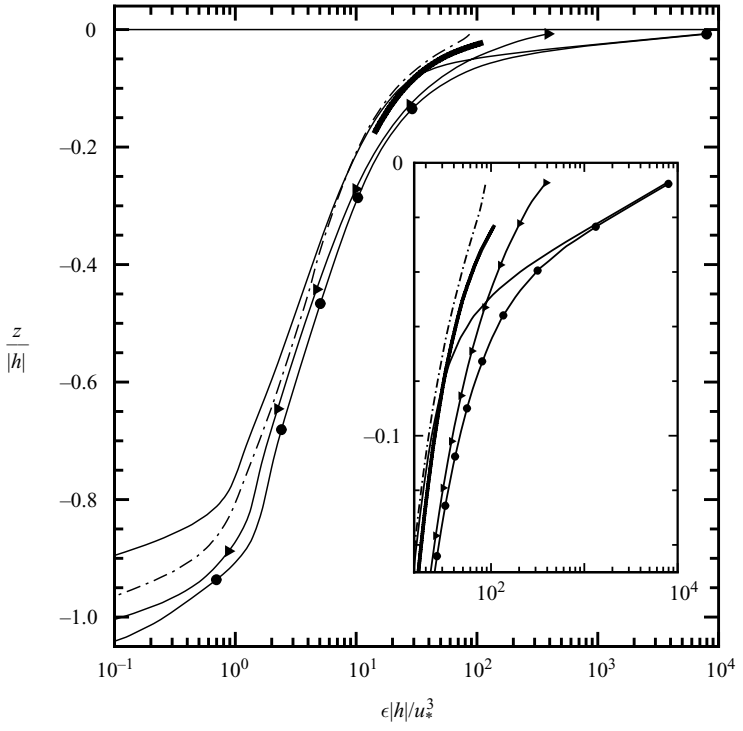


FIGURE 10. Profile of normalized dissipation $\epsilon|h|/u_{*o}^3$ for simulations with: no wave effects, dash-dot line; Stokes drift only, ►; breaking only, solid line; Stokes drift plus breaking, •; fully-developed wind waves. Dissipation is estimated from the subgrid-scale parameterization $\epsilon = C_\epsilon e^{3/2}/\Delta$ with $C_\epsilon = 0.93$. The heavy black line is the rough wall layer scaling $\epsilon = u_{*o}^3/0.4|z|$. The inset is a blow-up near the surface.

the enhancement of the SGS energy by breaking. Note in the region $0 > z/|h| > -0.05$ breaking is overwhelmingly the dominant source of SGS energy. Below a depth $z/|h| < -0.1$ the simulations again segregate into two families based on the presence or absence of the vortex force as Langmuir cells are depth filling and enhance the TKE over the bulk of the mixed layer.

Turbulent dissipation is a metric, produced by observational datasets, often used to infer the impact of waves on ocean currents, e.g. Terray *et al.* (1996), Drennan *et al.* (1996), Terray, Drennan & Donelan (1999). These field measurements report elevated dissipation by 1–2 orders of magnitude compared to (atmospheric) wall scaling $\epsilon \sim 1/z$ with the magnitude dependent on wave state. This increase is most often attributed to breaking waves. Previous LES with the vortex force driven by uniform stress also find enhanced dissipation near the water surface, and thus it is interesting to examine the relative contributions of Langmuir cells and breaking waves to dissipation in the present solutions. The turbulent dissipation from cases with uniform stress and different combinations of vortex force and wave breaking are compared in figures 10 and 11. Here we use the traditional SGS parameterization $\epsilon = C_\epsilon \mathrm{e}^{3/2}/\Delta$ (Moeng 1984) as a measure of net dissipation in our simulations. The LES driven by uniform stress and no wave effects reasonably reproduces the rough wall estimate $\epsilon = u_{*o}^3/\kappa|z|$, where $\kappa = 0.4$.

In our modeling, breaker work is strongly intermittent in space and time with its magnitude dependent on the phase speed c of any particular breaker. As a

https://doi.org/10.1017/S002211200700897X Published online by Cambridge University Press

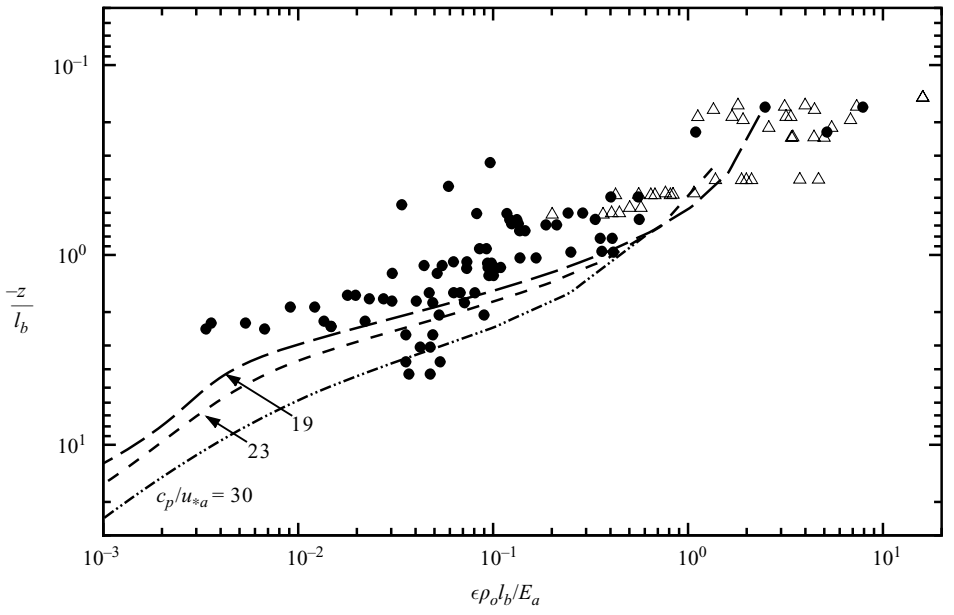


FIGURE 11. Near-surface normalized dissipation $\epsilon\rho_o l_b/\mathscr{E}_a$ for simulations with breaking and Stokes drift for varying wave age; $c_p/u_{*a} = 30$, dash-dot line; $c_p/u_{*a} = 23$, dashed line; and $c_p/u_{*a} = 19$, long-dashed line. The measurements of Terray *et al.* (1996) and Drennan *et al.* (1996) are indicated by • and △, respectively. In these data the length scale $l_b = c_p^2/g$, where c_p is the peak in the measured wave height spectrum for wind waves. In the LES, $l_b = c_E^2/g$, where c_E is the phase speed of the peak in the breaker energy flux spectrum.

consequence of (4.1*b*), all SGS variables including ϵ inherit these dependencies and considerable averaging is required to obtain reliable dissipation estimates. Below a depth $z/|h| < -0.2$ the dissipation profiles for all cases are similar in shape, and the results with the vortex force are only modestly elevated compared to cases with no Stokes drift. However, near the water surface the magnitude and vertical distribution of dissipation depend strongly on breaking and the vortex force. With breaking and Stokes drift the dissipation close to the water surface is more than (80, 2) times larger than values obtained from simulations with no wave effects and Stokes drift only, respectively. Enhanced dissipation is primarily a consequence of breaking, which is expected based on the high values of TKE shown in figure 8. Figure 11 compares dissipation estimates from LES with varying wave age in the non-dimensional variables (z/l_b) and $(\epsilon l_b\rho_o/\mathcal{E}_a)$ proposed by Terray *et al.* (1996) and Drennan *et al.* (1996), where l_b is a characteristic length scale of the wave field. In the field observations ϵ is obtained from velocity spectra in the inertial subrange, and the majority of the measurements were obtained under developing seas (wave age < 8) with significant wave heights $H_s < 0.5$ m. The data of Drennan *et al.* (1996) are more developed $c_p/u_{*a} < 23$ with $H_s \sim 0.88{-}2$ m. In terms of significant wave height, all the data are well below the estimate for fully developed waves discussed in § 2.1 (Alves *et al.* 2003). Drennan *et al.* (1996) note the choice of length scale in the dissipation scaling law is not unique; they plot their results using $l_b = H_s$ and $l_b = c_p^2/g$, where c_p is the peak in the wave-height spectrum excluding swell. The statistical variations in the observations are large, the range of conditions is small and an optimum length scale is not obvious from the data. These uncertainties make a direct comparison with

https://doi.org/10.1017/S002211200700897X Published online by Cambridge University Press

the present LES results obtained at higher wind speeds difficult. However, to illustrate the trends we show the LES results normalized using a length scale $l_b = c_E^2/g$, where c_E is the phase speed of the peak in the breaker energy-flux spectrum (see figure 3). The qualitative comparison between the observations and the LES with breakers and Stokes drift is good. As the wave age decreases from wind–wave equilibrium the LES results tend to limiting values, independent of c_p/u_{*a}, in agreement with the Terray *et al.* (1996) scaling arguments. A wider range of observational datasets is needed to test the LES predictions.

6.3. *Flow structures*

The statistical moments discussed in the previous sections are evidence of the influence of surface waves on the bulk properties of the mixed layer. Extensive visualization of the various flows is next discussed to elucidate further the spatial and temporal effects of vortex force and breaking on mixed-layer dynamics. Here the vertical velocity field is used as a marker to identify coherent structures in the flow. Figure 12 compares w-contours near the water surface for flows with different combinations of uniform stress or breaking and vortex force. The baseline simulation with no breaking and no vortex force shows that randomly distributed turbulent eddies dominate the near-surface motions, as is typical of a flat plate boundary layer. Intermittent breaking alone modifies this pattern in a manner consistent with our previous DNS: each breaker generates a forward and downward impulse and a weaker positive return flow. The breaker flow structures scale with the phase speed c and the number of events is consistent with the PDF of breaking. The relatively benign patterns in figures 12(a) and (c) are strongly modulated by the vortex force. Streamwise elongated patterns appear in figures 12(b) and (d) and the downwelling and upwelling lines reflect the formation of Langmuir cells. Closer inspection of the patterns reveals streamwise mergers at forward-looking Y-junctions, a consequence of the merger of positive and negative signed streamwise vortices from neighboring cells. The overall strength of the downwelling and upwelling lines is consistent with the high levels of vertical-velocity variance shown in figure 9. The life cycles of Langmuir cells for mixed layers driven by uniform stress are fully discussed by McWilliams *et al.* (1997).

There is a subtle hint in the images of figure 12 that intermittent breaking weakens the formation of Langmuir cells generated under uniform wind stress. In order to expose this breaker–vortex-force interaction we show w-contours from four different simulations with the same Stokes drift field at two different z-levels (figures 13 and 14). These images illustrate an impact of breaking on Langmuir-cell formation near the water surface ($0 > z > -2$ m) and also surprisingly deeper in the water column ($z \sim -13$ m). Overall, as the level of intermittent forcing increases (or equivalently as the wave age decreases) the spatial organization of the Langmuir pattern decreases; the lateral distance between downwelling lines becomes wider; and the lines shorten in length in the streamwise direction. These trends are especially apparent if we compare figure 13(a) and figure 13(d), which are simulations driven by uniform stress and by large intermittent breakers, respectively. Also in the simulation with the youngest waves (wave age $c_p/u_{*a} \sim 19$) the downwelling is strongly focused at Y-junctions. The spatial structure and sparsity of downwelling lines suggest that intermittent breaking alters the formation of Langmuir cells compared to the uniform stress case. The near-surface w-patterns are consistent with the changes in turbulent variances discussed previously.

The flow visualization in figure 14 shows unexpected flow patterns for simulations with and without breaking (and Stokes drift) well below the surface layer, $z \sim -13$ m.

https://doi.org/10.1017/S002211200700897X Published online by Cambridge University Press

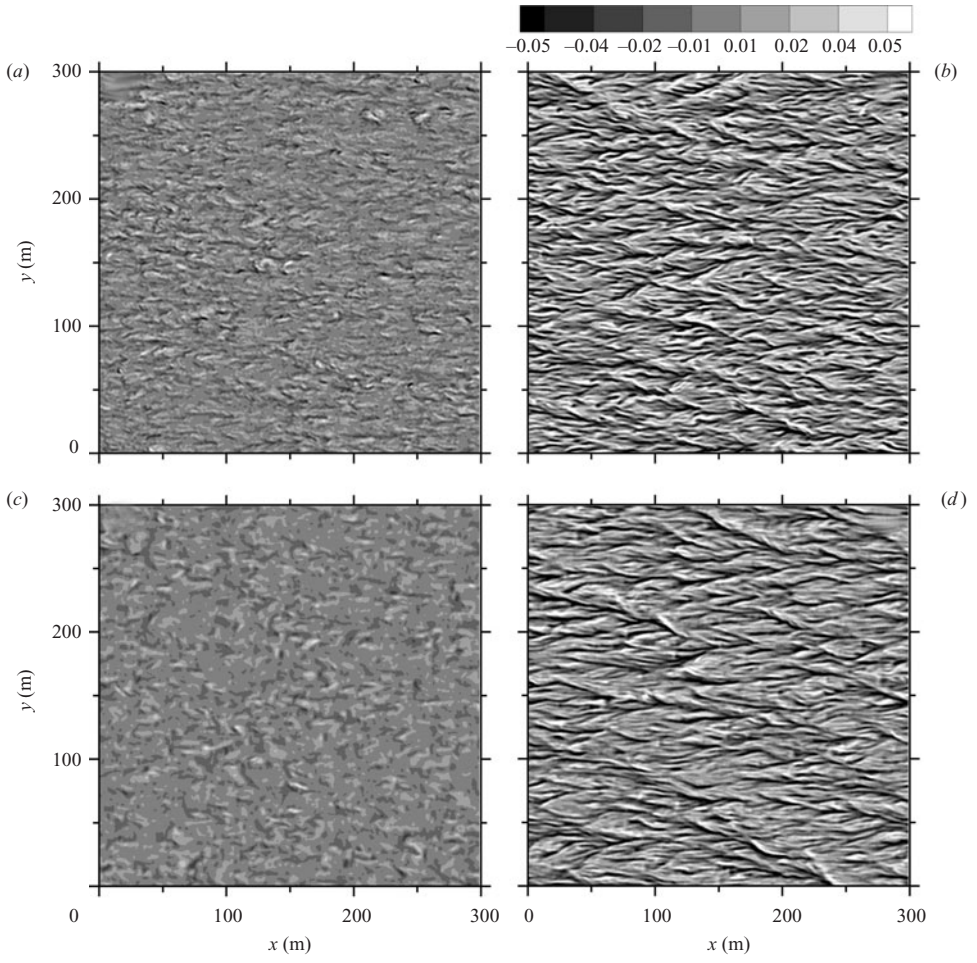


FIGURE 12. Snapshot of vertical velocity $\overline{w}$ at $z = -1.14$ m for different combinations of Stokes drift and wave breaking for fully developed waves $c_p/u_{*a} = 30$: (*a*) no wave effects and uniform stress, (*b*) uniform stress plus Stokes drift, (*c*) breaking waves and no Stokes drift, and (*d*) breaking waves plus Stokes drift. The grey-scale bar shown at the top of the figure is in units of metres per second.

For flows driven by uniform stress or weak intermittent breaking (figure 14*a* and 14*b*) broad horizontal streaks appear, and the streaks are rotated to the right of the surface wind by Coriolis effects (n.b., mean current profiles in figure 5). These patterns are signatures of depth-filling Langmuir circulations and are observed in all LES of the OBL driven by uniform stress and vortex force (e.g. Skyllingstad & Denbo 1995; McWilliams *et al.* 1997; Noh *et al.* 2004). However, this pattern remarkably changes when the surface forcing shifts to larger and more intermittent breaking. The streaky pattern is less organized as coherent round 'spots or jets' of concentrated negative w appear.

6.4. *Action of vortex force on breaker vorticity*

The intriguing interactions between breaking and vortex force shown in figures 13 and 14, supported by other visualization, motivated a search for the source of downwelling jets in LES. Numerous simulations with different PDFs of breaking show that these

https://doi.org/10.1017/S002211200700897X Published online by Cambridge University Press

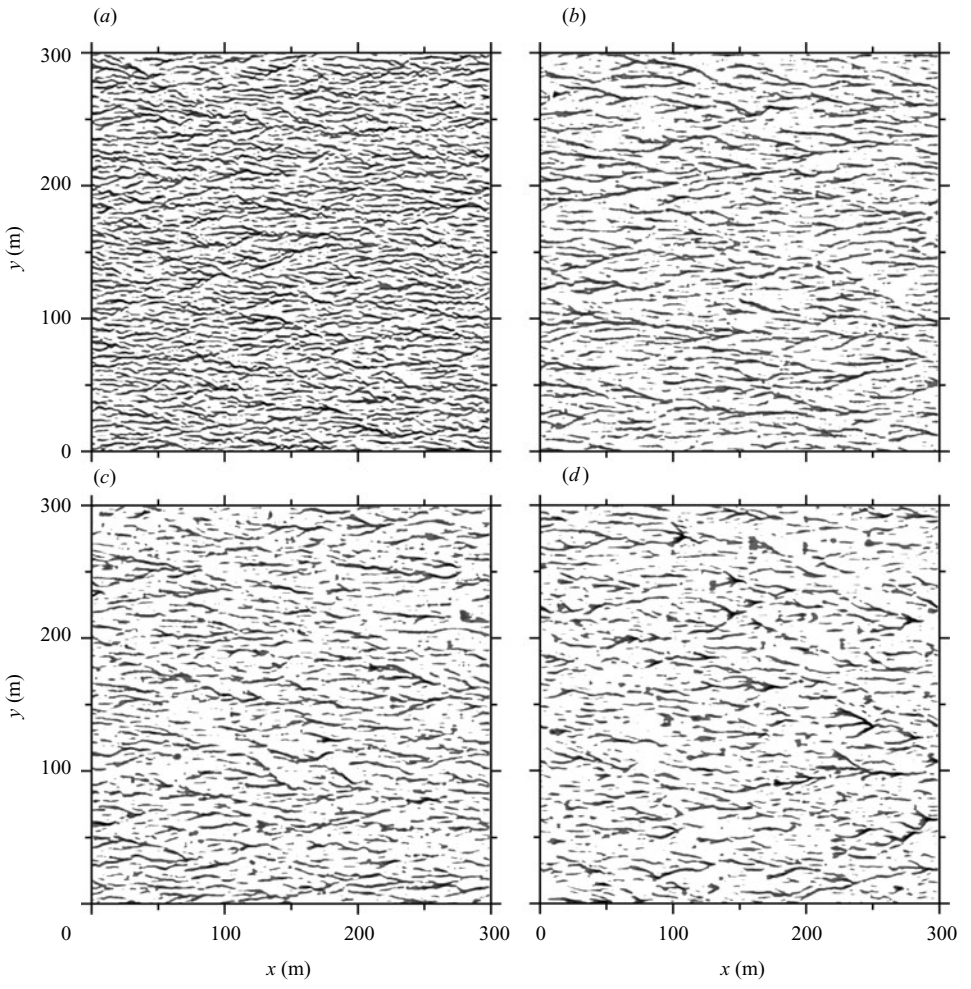


FIGURE 13. Contours of downwelling velocity $\overline{w} \leqslant -0.01$ m s^{-1} at $z = -0.38$ m for cases with Stokes drift and varying wave age: (*a*) uniform stress no breaking, (*b*) fully developed waves $c_p/u_{*a} = 30$, (*c*) $c_p/u_{*a} = 23$, and (*d*) $c_p/u_{*a} = 19$.

downwelling jets are robust features. For a given value of Stokes drift (or wind speed and wave age) they appear most often when the forcing is dominated by large intermittent breakers. Results with a PDF that emphasizes large-scale breaking are given in Sullivan *et al.* (2005).

Our present interpretation for the development of downwelling jets is based on a delicate coupling of breaker vorticity and the so-called CL2 instability mechanism (Leibovich 1983, p. 402) sketched in figure 15. CL2 is a potent pathway to generating Langmuir circulations that depends on positive feedback between the vortex force and local perturbations of horizontal current. For example, Nepf *et al.* (1995) speculate that wave breaking in their channel flow may provide 'seed vorticity' for the initiation of the CL2 mechanism. However, their results are made ambiguous by the presence of other transverse structures in their wavy flow, and the large influence of the bottom boundary layer in the shallow channel with surface wavelengths comparable to, or even larger than, the channel depth. Earlier, Csanady (1994) had speculated

https://doi.org/10.1017/S002211200700897X Published online by Cambridge University Press

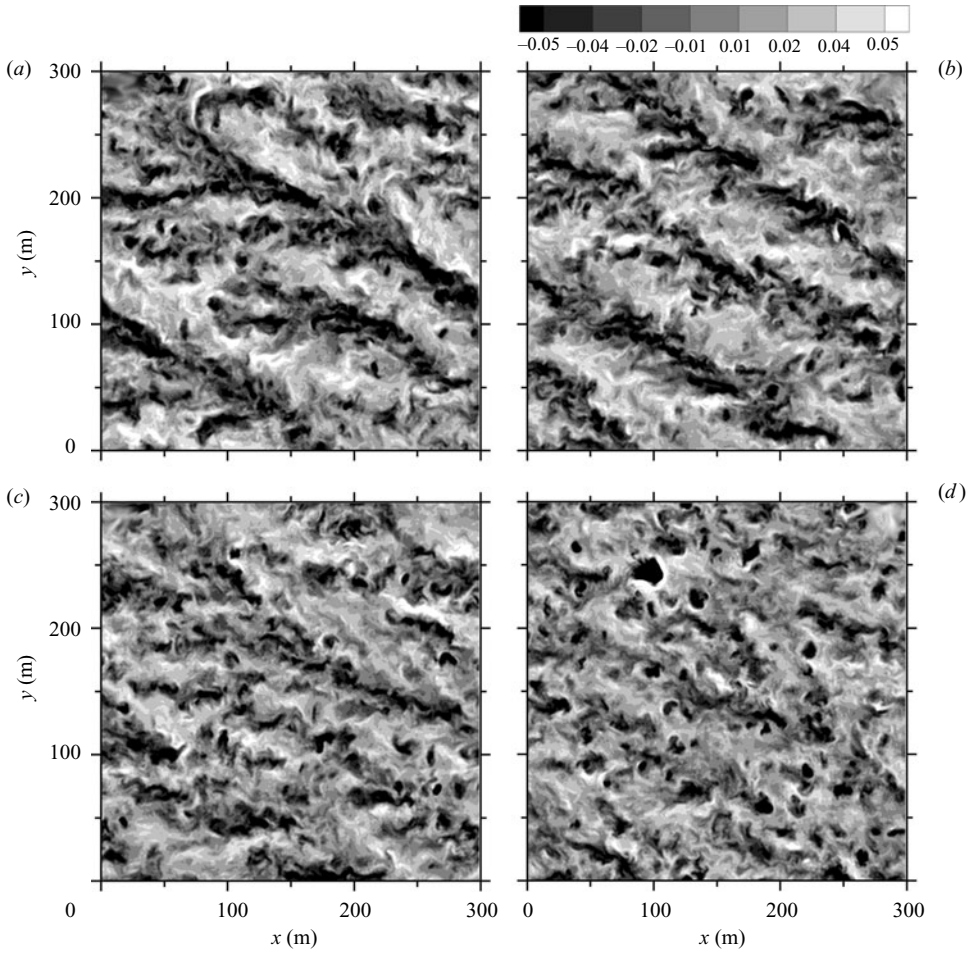


FIGURE 14. Vertical velocity contours at $z = -13.38$ m for the same flows as in figure 13. Note the appearance of the coherent round downwelling jets in (*c*) and (*d*). The grey-scale bar shown at the top of the figure is in units of metres per second.

that surface stress anomalies of finite extent, due to either wind gusts or breaking waves, might lead to a 'forced CL2 mechanism', with Stokes drift tilting the lines of vertical vorticity at the edges of the anomaly, without the need for the feedback of the CL2 mechanism. The idealized sequence of CL2 events (see figure 15) assumes a streamwise current fluctuation u' of finite y-extent and a Stokes drift u^{St} and requires no coherent surface-wave structure. First, the current anomaly generates vertical vorticity of opposite signs that lead to opposing vortex forces $u^{St}\overline{\omega_3}\,\hat{\mathbf{y}}$ that decay with depth providing the torque to generate counter-rotating vortices. Then the action of the vortex forces directed inward towards the centerline of the current fluctuation reinforces the perturbation and promotes the instability. The flow convergence at the surface leads to downwelling. In the original description of CL2 Leibovich (1983, p. 399) states 'Vorticity in the water body may arise from currents whose origins are unspecified, or ... by an applied wind stress ...'. We find the intensity, scale and proximity of the vorticity generated by breaking are important variables to be considered in CL2. These dependences might be anticipated since figure 15 is an

https://doi.org/10.1017/S002211200700897X Published online by Cambridge University Press

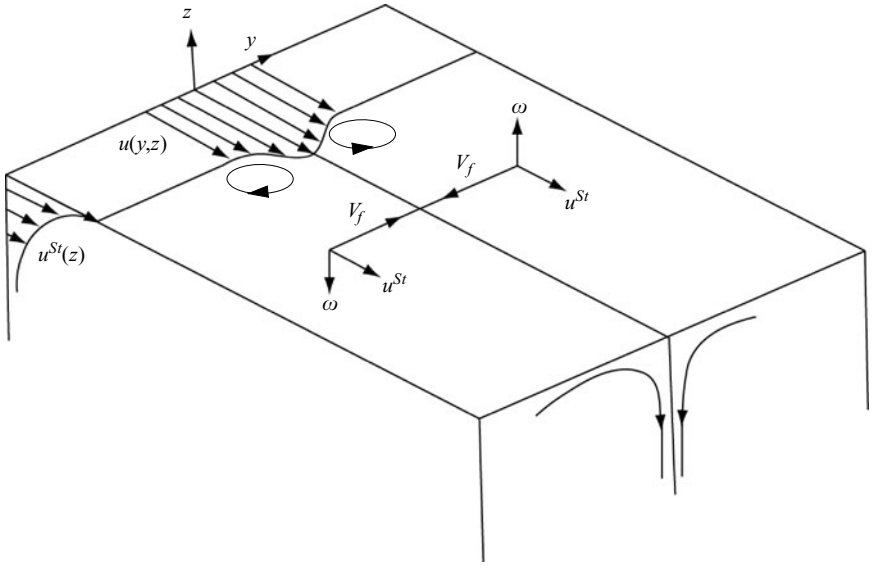


FIGURE 15. Sketch illustrating the CL2 instability mechanism for the generation of Langmuir circulations at the water surface, adapted from Leibovich (1983). The current perturbation $u(y, z)$ generates vertical vorticity $\omega\hat{\mathbf{z}}$ that is amplified by the vortex force $V_f = u^{St}\omega\hat{\mathbf{y}}$ that leads to downwelling at a convergence line. Breaking waves are a source of the initial streamwise current perturbation and vertical vorticity.

idealization of a single isolated perturbation, and thus this picture cannot be expected to predict new dynamics arising from the coupling of nearby strong CL2 events.

To illustrate the importance of background vorticity on Langmuir dynamics we compare vertical-vorticity fields from simulations driven by uniform stress and by intermittent breaking in figure 16. In the former case the vorticity is uniformly distributed in space, relatively weak and of small scale. In contrast, in the simulation with breaking the vertical vorticity is stronger in magnitude and contains a spectrum of large and small scales. An important point to notice is that each breaker generates both positive and negative vertical vorticity in close proximity that ideally interacts with the Stokes drift in the vortex force to generate strong local lateral convergence. Inspection of the contours and animations shows that as time advances the initial vertical vorticity field from each breaker evolves into multiple pairs of plus-minus signed vorticity, all of which merge at a vigorous forward looking Y-junction; the magnitude of downwelling at a Y-junction with breaking exceeds values obtained under uniform stress. The dynamics in figure 16 gives rise to the different patterns of convergence lines shown in figure 13.

Previous studies have found that breaker turbulence can persist for multiple wave periods (Melville *et al.* 2002; Sullivan *et al.* 2004) despite the limited lifespan of active breaking, a time scale of the order of the wave period $T = 2\pi c/g$. Thus it is interesting to examine the interaction between breaking turbulence and the vortex force for $t > T$. The post-breaking life cycle of vertical vorticity, vertical velocity and streamwise current for a typical breaking event extracted from a simulation is displayed in figures 17–19. The breaker scales are $\lambda \sim 20\,\mathrm{m}$, $c \sim 5.6\,\mathrm{m\,s^{-1}}$ and $T \sim 3.6\,\mathrm{s}$. The time and space evolution of the flowfields is qualitatively similar to the flow pattern sketched in figure 15 and illustrates that large breaking events seed the CL2 instability. However, complex dynamics can occur at merger points. At the

https://doi.org/10.1017/S002211200700897X Published online by Cambridge University Press

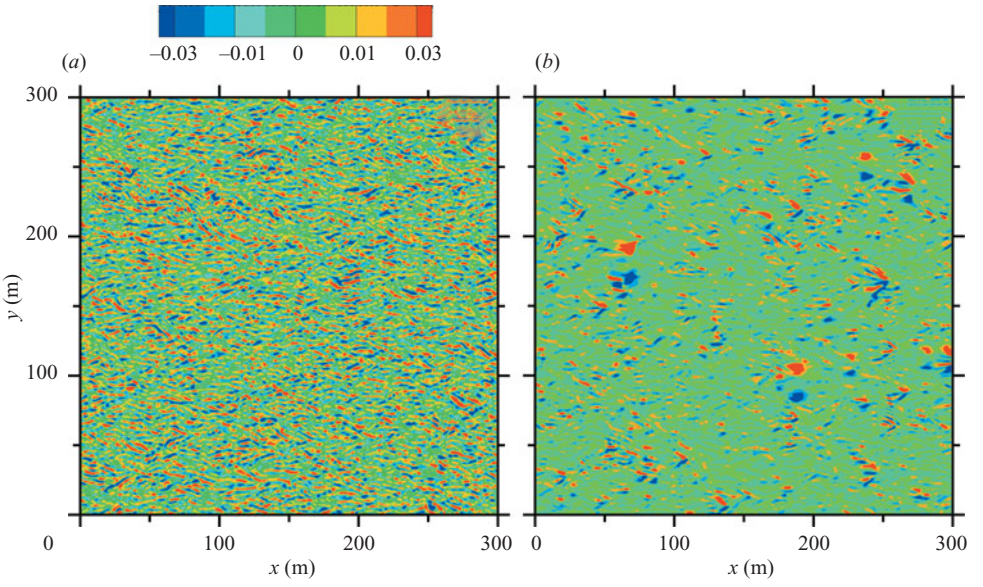


FIGURE 16. Snapshot of vertical vorticity $\overline{\boldsymbol{\omega}}\cdot\hat{\mathbf{z}}$ at $z = -1.14$ m for two simulations with Stokes drift driven by: (*a*) uniform stress and (*b*) breaking with wave age $c_p/u_{*a} = 19$. Note the paired plus and minus signed vertical vorticity that occurs at the lateral (y) ends of each breaker. The colour bar shown at the top of the figure is in units of per second.

initial time, the residual of a breaking event is a pair of vertically aligned vortices with a y-separation approximately equal to λ (we refer to these as the primary vortices). Each of the primary vortices amplifies and migrates towards a common centerline as a result of the vortex force. With increasing t, current perturbations and vortices internal to the primary pair develop as a result of CL2. This appears as an enhancement of the u-current at the internal edge of each primary vortex (see figure 17*b*,*d*). The new four vortex system grows in strength, propagates forward and heads to an inevitable collision at a forward location. However, notice the sign of the internal vortices is such that they collaborate to generate strong backflow (negative u) along the centerline of the vortex system retarding the forward motion of the breaker impulse. The flow response is vigorous downward motion. At late time, after about 80 s or 22 wave periods, the vortices all merge ending the event.

The response of the vertical velocity field at $z = -1.14$ m shown in figure 18 is consistent with the active movement of the vortices. Immediately after the breaking event w is laterally (y) distributed in front of and behind the breaker, a response to the forward impulse of breaking. As the CL2 instability grows a pair of downwelling lines develop just inside the primary outer vortices. The downwelling intensifies until at late time the lines join (intense Y-junctions are readily apparent in figure 13*d*). Upstream of the downwelling merger the u-currents slow and change sign as if in response to a stagnation point.

Deeper in the water column, $z \sim -13$ m, a round downwelling jet forms slightly forward and to the right of the surface breaking event. At this depth the jet first appears about 80–100 s after the breaking event. Its appearance is consistent with a travel time of $\mathcal{O}(100)$ s and a vertical velocity $w \sim -0.1$ m s^{-1}. Thus we are lead to conclude that the downwelling jets in figure 19 (and those in figure 14*d*) originate at the water surface and result from interactions between CL2 type instabilities. We

https://doi.org/10.1017/S002211200700897X Published online by Cambridge University Press

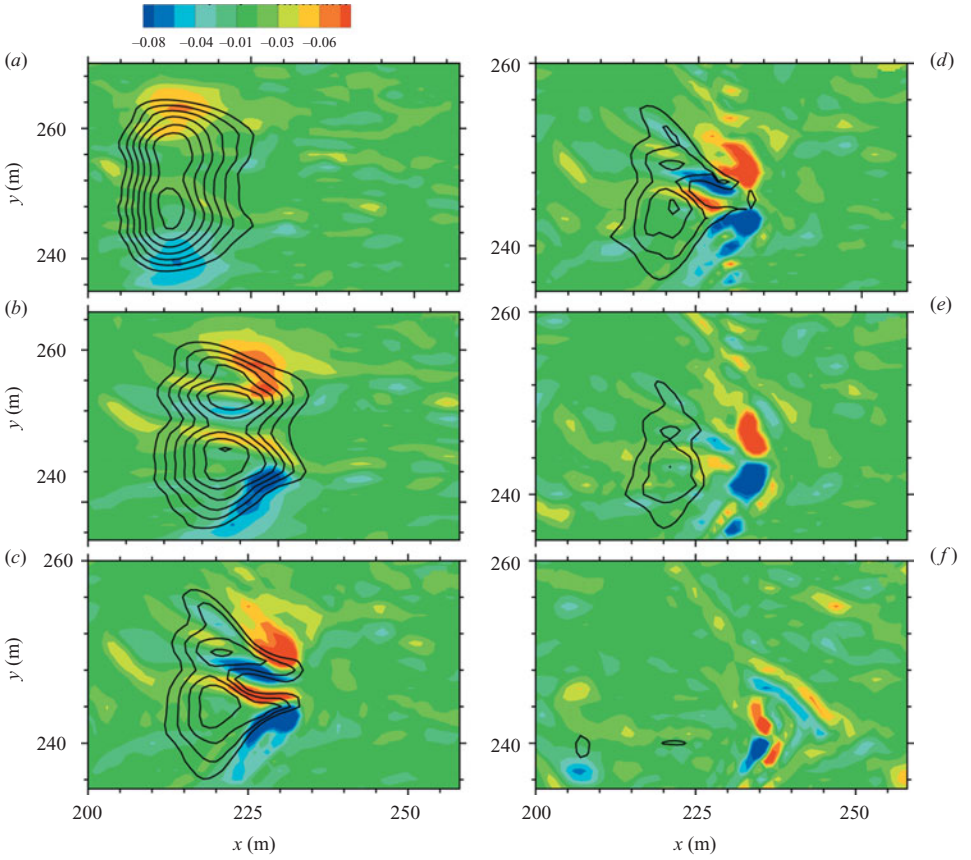


FIGURE 17. Temporal evolution of breaker flowfields under the action of the vortex force at $z = -1.14$ m for the simulation with wave age $c_p/u_{*a} = 19$. The resolved vertical vorticity $\overline{\boldsymbol{\omega}}\cdot\hat{\mathbf{z}}$ is shown in the colour images and the resolved streamwise current $\overline{u}$ as solid contour lines. The colour bar at the top of the figure is in units of per second and the contour lines are evenly spaced in the range $[0, 0.3]$ m s^{-1}. Relative to panel (a) the elapsed time in seconds is [18,(a)], [37,(b)], [44,(d)], [55,(e)], [80,(f)]. Note the expanded y-scale beginning with panel (c).

find that the scale and intensity of the downwelling jets varies as expected with the breaker phase speed c. With intermittent large-scale breaking the downwelling jets penetrate well below the surface layer and alter the structure and mixing of the OBL.

The flow patterns displayed in figures 17–19 are typical of strong breaking events. Breaking supplies seed vertical vorticity to start the CL2 instability, but the flow can rapidly degenerate into multiple pairs of vortices each acting under the influence of the vortex force. The forward propagating vortex system merges and produces downwelling. Thus surface interactions between breaker vorticity and vortex force lead to the formation of a new coherent structure below the surface layer. When the vertical-vorticity seeds of the CL2 instability are relatively weak, streamwise oriented vortices develop that evolve into classic Langmuir circulations. However, if the initial vorticity is strong, downwelling jets also develop and the surface Langmuir pattern is more intermittent. Our results show that turbulence from breaking and the CL2 mechanism play a role in an OBL with fully developed turbulence, a wave spectrum, and realistic currents.

https://doi.org/10.1017/S002211200700897X Published online by Cambridge University Press

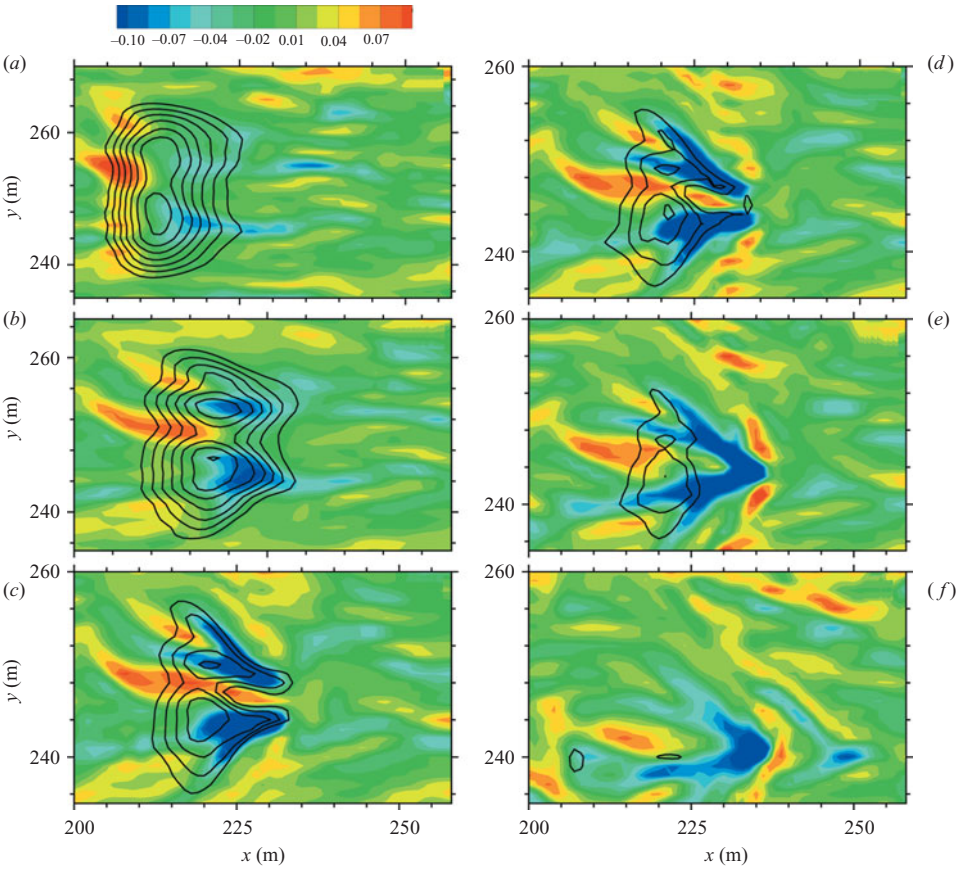


FIGURE 18. Temporal evolution of resolved vertical velocity $\overline{w}$ and streamwise current $\overline{u}$ for the same time periods and spatial locations as in figure 17. The colour bar at the top of the figure is in units of metres per second.

The vertical velocity skewness $\langle \overline{w}^3 \rangle / \langle \overline{w}^2 \rangle^{3/2}$ is a bulk statistical measure often used to detect the presence of coherent structures in a boundary-layer flow. For example, Moeng & Rotunno (1990) find that a bias in vertical velocity skewness indicates the presence of thermal plumes in a convective flow. Figure 20 shows vertical velocity skewness from our simulations with different combinations of breaking and vortex force. In all cases with intermittent breaking and vortex force the skewness is more negative than the comparable case driven by uniform stress and Stokes drift. In the absence of the vortex force the skewness is only slightly negative. The large negative skewness in simulation $B3+St$ reflects the presence of vigorous downwelling jets discussed above. Notice in this simulation, the skewness is persistently negative well below the surface layer indicating that once the downwelling jets develop at the surface they persist throughout the mixed layer. This is additional evidence that strong intermittent breaking and the vortex force can act synergistically to form a coherent structure roughly analogous to a thermal plume. The bias towards negative skewness, induced by surface waves, appears to be robust across wind speed as a simulation at $U_a = 30$ m s^{-1} shows a similar trend, with further discussion in § 7.

https://doi.org/10.1017/S002211200700897X Published online by Cambridge University Press

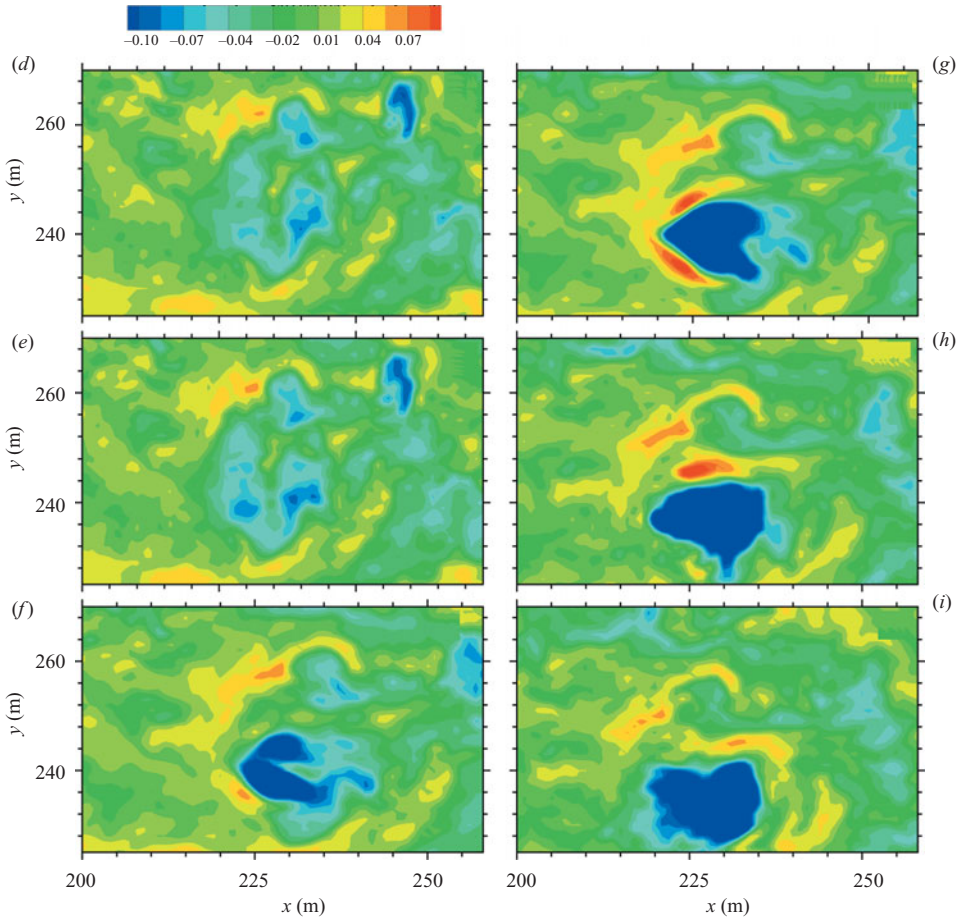


FIGURE 19. Time history of vertical velocity $\overline{w}$ at $z = -13.38$ m for the same flow conditions as in figures 17 and 18. Relative to figure 17(a) the elapsed time in seconds is [44,(d)], [55,(e)], [80,(f)], [90,(g)], [117,(h)], [143,(i)]. The colour bar at the top of the figure is in units of metres per second. At this depth the downwelling jet forms at nearly the same horizontal location as the breaking event in figure 17, but begins to appear 80–90 s later.

6.5. *Scalar statistics and mixed-layer depth*

The importance of surface waves to OBL dynamics and scalar transport is traditionally assumed to be confined to a depth on the order of the wave height. However, these LES results clearly indicate that surface waves alter mixed-layer dynamics over a greater depth $\mathcal{O}(|h|)$, mainly due to the vortex force. Scalar transport is important in the mixed layer, especially so for OBLs under high wind conditions since entrainment cooling can alter the development of tropical cyclones (e.g. Emanuel 1999, 2004). This raises the important question of whether surface waves play an expanded role in scalar mixing.

Figure 21 illustrates the influence of surface waves on the bulk mixed layer temperature and the structure of the thermocline inversion. Averaged over identical periods, the mixed-layer temperature is cooler in the presence of vortex force due to more efficient entrainment at the thermocline. Compared to the cases driven by uniform stress or breaking only the simulations with vortex force also exhibit

https://doi.org/10.1017/S002211200700897X Published online by Cambridge University Press

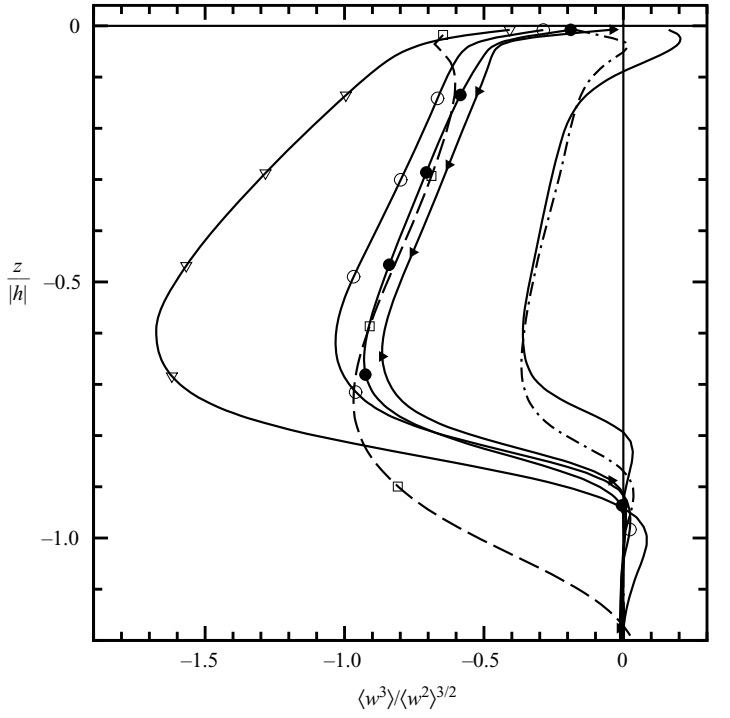


FIGURE 20. Profiles of vertical velocity skewness $\langle \overline{w}^3\rangle/\langle \overline{w}^2\rangle^{3/2}$: no wave effects dash-dot line; breaking-only wave age $c_p/u_{*a} = 30$, solid line; Stokes drift only, ►; Stokes drift plus breaking with wave age $c_p/u_{*a} = 30$, •; Stokes drift plus breaking with wave age $c_p/u_{*a} = 23$, ○; Stokes drift plus breaking with wave age $c_p/u_{*a} = 19$, ▽; and Stokes drift plus breaking with wave age $c_p/u_{*a} = 30$ for $U_a = 30$ m s^{-1}, □.

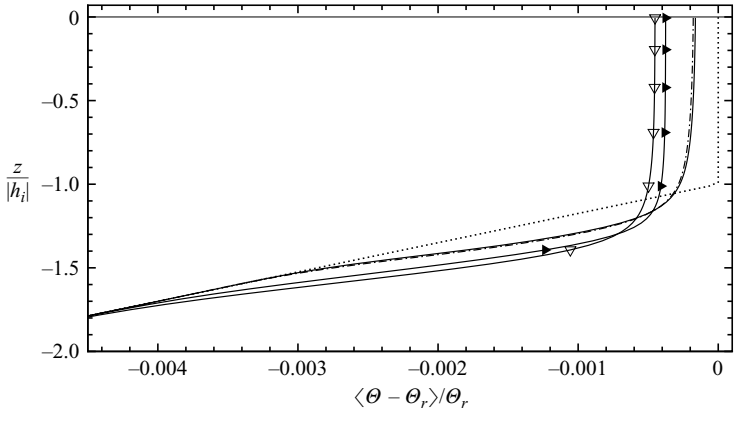


FIGURE 21. Profiles of normalized temperature for simulations: no wave effects, dash-dot line; breaking-only wave age $c_p/u_{*a} = 30$, solid line; Stokes drift only, ►; and, Stokes drift plus breaking with wave age $c_p/u_{*a} = 19$, ▽. The mixed-layer depth and temperature are normalized by the initial value $h_i = -32.4$ m and the reference temperature $\theta_r = 283.5$ K, respectively. The time averaging is over 10 000 s starting at $t = 40\,000$ s for each simulation. For reference, the initial mixed-layer sounding is shown as a dotted line. Notice how the temperature profiles from all simulations relax back to the initial sounding for $z/|h_i| \ll -1$.

https://doi.org/10.1017/S002211200700897X Published online by Cambridge University Press

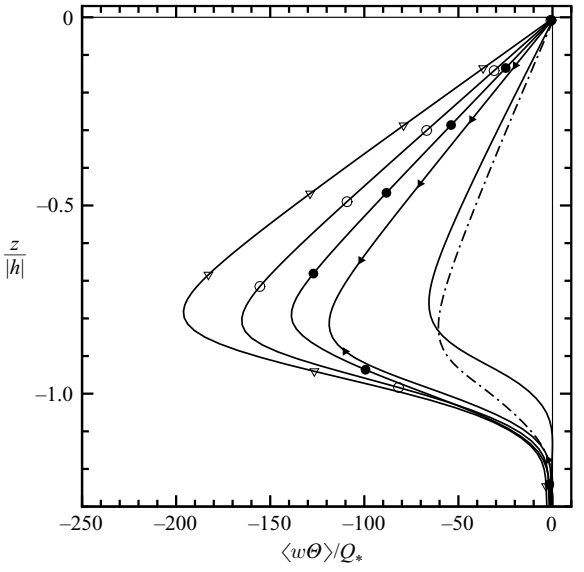


FIGURE 22. Profiles of vertical (total) scalar flux normalized by the surface value Q_* for simulations: no wave effects, dash-dot line; breaking only wave age $c_p/u_{*a} = 30$, solid line; Stokes drift only, ►; Stokes drift plus breaking with wave age $c_p/u_{*a} = 30$, •; Stokes drift plus breaking with wave age $c_p/u_{*a} = 23$, ○; and Stokes drift plus breaking with wave age $c_p/u_{*a} = 19$, ▽.

sharper temperature gradients in the entrainment zone. In these simulations vigorous turbulence generated by the combined action of Langmuir circulations and breaking overshoots the mean entrainment height leading to a stiffer inversion; this is analogous to entrainment dynamics in the daytime convective atmospheric boundary layer (Sullivan *et al.* 1998). Thus our simulations show that surface waves can modulate the structure of the OBL entrainment zone. This is further illustrated in figure 22 where we compare vertical profiles of total average scalar flux $\langle\overline{w\theta'}\rangle$ for our suite of simulations. Recall, the same small surface flux Q_* is imposed in all simulations. As expected for these neutrally stratified OBLs, scalar mixing is dominated by entrainment dynamics. The increase in entrainment in the simulations with the vortex force shows that surface waves do indeed enhance mixing in the OBL compared to a baseline simulation with no Stokes drift. This is largely a consequence of depth-filling Langmuir cells that promote mixing, but also because the Langmuir cells alter the structure of the current profiles near the thermocline (Skyllingstad 2005), i.e. the Langmuir cells alter the current shear near $z \sim h$. The downwelling jets in simulation $B3 + St$ are also observed to play a critical role in setting the scalar mixing efficiency of the OBL; the entrainment flux is largest in this simulation. The entrainment of cooler water from below the thermocline can increase by almost a factor of 4 in the simulations with both wave breaking and Stokes drift compared to the baseline simulation with no wave effects. At the same time, surface waves enhance the scalar variance as shown in figure 23. The Langmuir cells (and downwelling jets) generated by surface waves alter the shape of the thermocline temperature profile and potentially are powerful enough to excite internal gravity waves (Chini & Leibovich 2003). These results are not impacted by the SGS model for scalar flux. For the simulations $\langle\overline{w\theta'}\rangle_{sgs}$

https://doi.org/10.1017/S002211200700897X Published online by Cambridge University Press

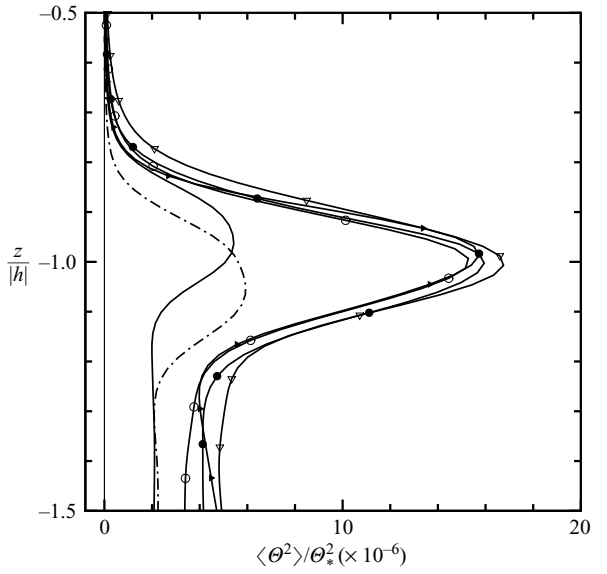


FIGURE 23. Scalar variance profiles for simulations with: no wave effects, dash-dot line; breaking only wave age $c_p/u_{*a} = 30$, solid line; Stokes drift only, ►; Stokes drift plus breaking with wave age $c_p/u_{*a} = 30$, •; Stokes drift plus breaking with wave age $c_p/u_{*a} = 23$, ○; and Stokes drift plus breaking with wave age $c_p/u_{*a} = 19$, ▽. The normalizing parameter $\Theta_* = Q_*/u_{*o}$.

referenced to the maximum entrainment flux in figure 22 peaks at 15% at $z/|h| \sim -1$ and over the bulk of the mixed layer $-0.9 < z/|h| < 0$ is less than 5%.

7. Wind speed dependence

The preceding LES results for a wind speed of 15 m s^{-1} clearly demonstrate that OBL dynamics and mixing depend on the structure and state of the surface wave field, through the wave height and breaker spectra. These spectra vary with U_a (and for a fixed wind also with wave age c_p/u_{*a}), so it is important to consider how the results might change for lower and higher winds, and in situations of wind–wave disequilibrium as the latter is the more probable state of winds and waves. Future LES will more fully quantify these dependences, but we make some preliminary estimates assuming the empirical formulas in §§ 2 and 3 hold, in particular that the Froude scaling is valid for different U_a. Ideally for an LES posing we need both the U_a and c_p/u_{*a} dependence of the Stokes drift, the atmospheric momentum and energy fluxes and the breaker spectrum. We are also interested in large values of U_a, where imagery of the sea surface shows impressive breaking events, and OBL dynamics regulating the sea-surface temperature are especially critical for tropical cyclone evolution.

First, the relative importance of Stokes forcing compared to wind stress depends on the turbulent Langmuir number $L_{at} = \sqrt{u_{*a}/u^{St}}$ (McWilliams *et al.* 1997) with the importance of conservative wave–current interactions increasing with decreasing L_{at}. Li, Garrett & Skyllingstad (2005) extensively explore the parameter space spanned by buoyancy, shear and Stokes forcing using LES, and for typical oceanic conditions find the OBL is in a regime dominated by Langmuir turbulence $L_{at} \sim 0.3$, i.e. wave–current interactions are important. To test this L_{at} scaling in the presence of

https://doi.org/10.1017/S002211200700897X Published online by Cambridge University Press

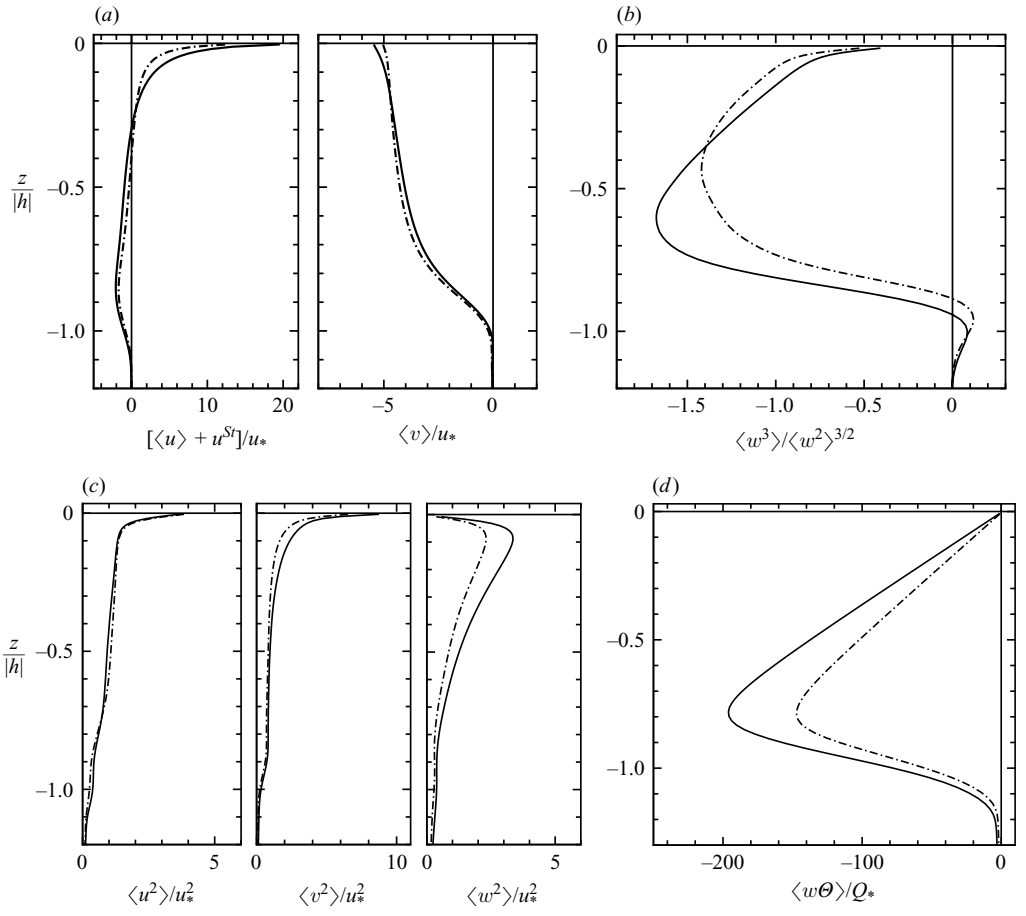


FIGURE 24. The impact of varying Stokes drift on: (*a*) mean currents, (*b*) vertical velocity skewness, (*c*) turbulence variances, and (*d*) scalar flux. The solid line in each figure is the result using the wave equilibrium spectrum given by (2.1) and the dotted line is the result for a fetch-limited wave-height spectrum given by Komen *et al.* (1994, p. 187) with wave age $c_p/u_{*a} \sim 19$. The magnitude of the Stokes drift u^{St} for the fetch-limited spectrum is reduced by about a factor of 2 compared to the equilibrium spectrum.

intermittent breaking waves an LES identical to $B3 + St$ is performed but with a reduced value of Stokes drift corresponding to growing seas with wave age $c_p/u_{*a} = 19$ (case $B3 + FSt$ in table 1). In this LES, the Stokes drift profile is computed from the empirically determined fetch-limited wave spectrum given by Komen *et al.* (1994, p. 187). This is a severe test of the solution robustness as u^{St} is reduced by more than a factor of 2 in the upper part of the mixed layer when the wave age varies from 30 to 19; this change in wave age implies L_{at} increases by $\sqrt{2}$. A comparison of various statistical moments from simulations $B3 + St$ and $B3 + FSt$ is given in figure 24.

The overall impression from these results is that changing the Stokes forcing by a factor of 2 does not alter the basic qualitative behavior of the OBL. The shape of the current profiles, enhanced spanwise variance and large entrainment flux are evidence that wave–current interactions and breaker forcing are important to the flow dynamics over a wide range of sea states. Flow visualization of the w-current (not presented) clearly shows streamwise oriented Langmuir circulations and the

https://doi.org/10.1017/S002211200700897X Published online by Cambridge University Press

formation of downwelling jets in simulation $B3 + FSt$ similar to those in $B3 + St$. The negative bias in the vertical velocity skewness in figure 24 reflects the presence of these coherent structures. Although clearly not exhaustive, our solutions appear reasonably robust to changes in Stokes forcing and further support the L_{at} scaling proposed by McWilliams *et al.* (1997) and verified by Li *et al.* (2005) in the presence of breaking waves.

To investigate the wind speed dependence further we next utilize the formula in § 2, $u_{*a} \sim \sqrt{C_d} U_a$ and $u^{St} \sim 1/f_p$ or $\sim U_a$. Therefore the turbulent Langmuir number has a weak wind speed variation because of the drag dependence $L_{at} \sim C_d^{0.25}$. For $U_a =$ 15 m s^{-1} and the Stokes velocity at $z = 1$ m, we estimate $L_{at} = 0.3$, which is a regime where Stokes forcing is important (see also McWilliams *et al.* 1997; Li *et al.* 2005). Doubling the wind speed to 30 m s^{-1} increases the drag coefficient $C_d = 2.3 \times 10^{-3}$ and therefore $L_{at} = 0.33$. At even higher winds, $U_a > 30$ m s^{-1}, C_d is probably wind speed independent or even decreasing (Donelan *et al.* 2004), which again implies $L_{at} \sim 0.3$. Based on the above scaling we conclude for all winds greater than 15 m s^{-1} the vortex force should remain significant relative to the wind stress.

Estimating the high wind speed dependence of the breaker spectrum is far less certain due to the sparsity of field data. In §§ 2 and 3 we use bulk momentum and energy conservation arguments along with data from Terray *et al.* (1996), Melville & Matusov (2002), Melville *et al.* (2002) in the wind speed range $U_a \sim 7$–15 m s^{-1} to build a breaker distribution with U_a and c_p/u_{*a} dependences. We now assume these scaling arguments hold at higher winds. The critical trends for the breaker distribution are given in figures 1–3. The peak phase speeds (or scales) for momentum and energy transfer (c_τ, c_E) from breaking move closer to the peak in the wave-height spectrum with increasing wind speed and decreasing wave age (figure 3). An estimate for the peak scale for breaker momentum can be obtained by noticing that the integrand of (3.16) changes sign at a crossover point $c \sim g_t u_{*a}$. Using this as an estimate for c_τ yields

$$c_\tau/c_p \;\approx\; 2\pi\, \nu\, g_t\, u_{*a}/U_a \quad \text{or} \quad c_\tau/c_p \approx g_t \sqrt{C_d}\,, \tag{7.1}$$

which shows a slightly superlinear dependence of breaker momentum on wind speed (contained in c_p and the drag coefficient) and linear dependence on wave age (contained in the Terray parameter).

Based on the above arguments the general conclusion is that with increasing U_a the vortex force remains roughly constant and the importance of intermittent breaking increases. Results from LES at $U_a = 30$ m s^{-1}, outlined in § 5, support these scaling arguments. The vertical velocity skewness in figure 20 at double the wind speed has a local minimum near the surface and a broad region near the thermocline, indicating the presence of coherent structures near $z \sim h$. Flow visualization indicates downwelling jets form at a wave age $c_p/u_{*a} \sim 30$ at this wind speed. (Recall that at lower winds the downwelling jets were either quite weak or nonexistent for the same value of c_p/u_{*a}.) This is a direct consequence of the shift to larger-scale more-intermittent breaking shown in the PDF $P(c)$ of figure 1. Compared with a baseline simulation with no wave effects, the entrainment of cool water at the thermocline increases by at least 30% due to wave processes, and this is likely to be consequential for the sea-surface temperature evolution.

https://doi.org/10.1017/S002211200700897X Published online by Cambridge University Press

8. Final remarks

8.1. *Conclusions*

A large-eddy simulation model of the OBL is described that accounts for surface wave effects through non-conservative breaking waves and phase-averaged conservative wave–current interactions. The equations for the resolved flow components are the Craik–Leibovich (CL) theory with crucial wave–current coupling through the vortex force. These equations are further augmented by a sum of discrete momentum impulses to model breaking. A broadband spectrum of waves, typical of measured conditions, is used to compute the Stokes drift profile which appears in the vortex force. The LES equations are closed using an eddy viscosity approach based on the subgrid-scale turbulent kinetic energy. The prognostic subgrid-scale TKE equation includes Stokes-drift production and breaker work terms that enhance subgrid-scale energy near the water surface. In this LES the traditional method of forcing an OBL by constant surface stress is replaced by a stochastic model that intermittently supplies momentum and energy to the underlying currents. The aggregate effect of breaking is a linear superposition of discrete events of varying scale with each event a time-varying three-dimensional impulse. The breaker model obeys Froude scaling and is designed to match laboratory and field observations. Matching the bulk momentum and energy fluxes between the atmosphere and ocean determines constants in the PDF of breaking, and the rate of breaking and its variation with wind speed and wave age are critical components of the model.

LES results at moderate wind speed $U_a = 15$ m s^{-1} illustrate how surface waves impact the dynamics and mixing in the OBL in important ways. Langmuir circulations are induced by the phase-averaged wave–current interactions, primarily through the vortex force. They are depth-filling; they increase the efficiency of vertical transport; and they enhance entrainment at the base of the thermocline. In an OBL driven by constant stress with a broad wave-height spectrum only small differences were found from previous LES that used a single dominant wave component. For fully developed waves the impact of intermittent breaking waves is mainly confined to the region close to the water surface; they energize the surface layer, destroy traditional wall layer scaling and enhance the turbulent dissipation.

Stochastically distributed breaking waves also disrupt the surface downwelling patterns, the characteristic signatures of Langmuir circulations. As the breaking becomes more intermittent and focused towards larger scales, the downwelling lines shorten in length and become more widely separated in the lateral direction. When downwelling lines join, they are sites of concentrated negative vertical velocity. For a given wind speed, fully developed equilibrium waves break often at small scales, while younger seas break more intermittently at larger scales closer to the peak in the wave-height spectrum. This wave-age dependence has consequences for the interaction between breaking and Langmuir circulations. Although the vortex force and breaking are added linearly to the equations, they can couple in a surprising way to generate a new coherent structure, a downwelling jet, which weakens but coexists with traditional Langmuir cells (i.e. in the absence of breakers). The origins of downwelling jets are surface breaking sites, and their formation is closely linked to the strength and scale content of the near-surface vertical vorticity field and the CL2 instability mechanism. Streamwise breaking and its associated strong vertical vorticity interacts with the vortex force over multiple wave periods. Breaking seeds the CL2 instability and generates strong lateral convergence at a location forward of the initial breaking site. The onset of downwelling jets coincides with a shift toward

https://doi.org/10.1017/S002211200700897X Published online by Cambridge University Press

larger-scale breaking, i.e. as the wind speed increases and/or the wave age decreases. The jets are found to extend throughout the mixed layer and can significantly alter the vertical velocity skewness. Wave processes are globally important as Langmuir circulations and downwelling jets enhance the entrainment of cool water at the OBL thermocline. In summary, OBLs are importantly different from their wall-bounded shear-layer counterparts because of surface waves. These effects need to be accounted for in bulk parameterizations of the OBL.

8.2. *Discussion*

There are several aspects of the LES predictions that invite further numerical evaluation and experimental testing. First, we adopt the asymptotic CL model of wave–current interactions with no feedback. Fully coupled current and wave fields might introduce transverse inhomogeneity that can potentially alter the Stokes drift and breaking distributions which are used in the present model. Work by Zhou (1999) and Kawamura (2000) indicates that CL is a valid approximation but further exploration is warranted. Next, the LES wave forcing and current response predictions need to be tested in field conditions for a variety of wind speeds and wave states. This has the advantage of validating the LES, but it can also help clarify the PDF of breaking and its dependence on environmental conditions. The LES results suggest wave processes are important at high winds, especially so for tropical cyclone evolution through enhanced entrainment of cool water at the thermocline. This needs to be checked with new instrumentation and focused field campaigns and additional explorations of the LES parameter space. The present LES results are an impetus to incorporate more fully wave influences in bulk models of the OBL such as the K-profile parameterization (Large *et al.* 1995; McWilliams & Sullivan 2000; Smyth *et al.* 2002; McWilliams & Huckle 2006).

Perhaps the greatest need is to improve the description of the breaking statistics as a function of wind speed, wave age and wind–wave misalignment. The statistical description of breaking used here is speculative, and may be criticized for its incompleteness, but we believe that the significance of the new dynamics that is introduced to OBL modeling by the explicit inclusion of both breaking and Langmuir turbulence justifies the sometimes crude assumptions made here. With very recent developments in both field measurements and modeling of surface waves and wave breaking, we expect that one of the next developments will be to use the output of wind–wave numerical models to describe the breaking statistics for the OBL, i.e. the coupling of OBL and wind–wave numerical models. We believe that the present results will provide guidance on addressing these developments.

We thank Edward Patton, Stephen Belcher, who contributed to this work through many informal discussions, Leonel Romero, for supplying us with wave-model computations, and the anonymous reviewers for their comments. Partial support for this work was provided by ONR grants N00014-00-C-0180 and N0001405IP20029 and NCAR Opportunity Fund for P. Sullivan, NSF DMS0327642 and ONR N00014-04-1-0166 for J. McWilliams, and ONR N00014-02-1-0249 and NSF CTS-02-15638,OCE-01-18449,OCE-02-42083 for K. Melville. NCAR is sponsored by the National Science Foundation.

https://doi.org/10.1017/S002211200700897X Published online by Cambridge University Press

Appendix. LES code details

A.1. *Numerical method with breakers*

The base set of LES equations for the resolved fields, subgrid-scale energy and pressure described in §4 are solved using a mixed finite-difference pseudospectral scheme with a third-order Runge-Kutta time stepping with a fixed Courant-Friedrich-Lewy (CFL) number. Solution variables are staggered in the vertical direction: $(\overline{u}, \overline{v}, \overline{\theta}, \overline{p})$ are located at cell centers while $(\overline{w}, e)$ are positioned at cell faces. Periodic lateral boundary conditions are assumed while a radiation boundary condition is imposed at the lower boundary ($z \to -\infty$) of the computational domain (Klemp & Durran 1983). The code is parallelized with the Message Passing Interface using vertical domain decomposition. The elliptic Poisson equation for pressure is solved with a custom built direct solver utilizing a parallel matrix transpose.

The simulation code is extensively modified to account for stochastic wave forcing. Observations of breaking waves in the equilibrium wind–wave regime report that the phase speed of detectable breakers varies from $c \approx 1$ to $c \approx 14$ m s^{-1} for wind speeds $7 < U_a < 15$ m s^{-1} (Melville & Matusov 2002). Based on the linear dispersion relation the breaker length scale λ then ranges from 0.6 m to more than 100 m, while its period T ranges from 0.6 s to more than 9 s. Capturing the breaker forcing adequately over this wide scale range requires careful evaluation of the impulse $\overline{A_i}$ in our integration scheme. From preliminary solutions we found that simply evaluating $\overline{A_i}(\boldsymbol{x}, t)$ and then inserting it into the right-hand side of our standard algorithm would completely miss or generate only a partial impulse. Hence, as the current fields moved forward in time they would either remain laminar or never become fully turbulent. The method successfully employed advances the current fields from stage n to stage $n+1$ in the Runge-Kutta scheme using the rule,

$$\overline{u}_i^{n+1}(\boldsymbol{x}) = \overline{u}_i^{n}(\boldsymbol{x}) + \Delta t \eta \left(r_i(\boldsymbol{x}) - \frac{\partial \overline{p}}{\partial x_i}(\boldsymbol{x}) + \overline{A}_i^{*}(\boldsymbol{x}, t) \right)^{n} + \cdots, \tag{A1}$$

where Δt is the time step, r_i denotes all other terms on the right-hand-side, of (4.1), η is a weight associated with the time stepping, and the dots indicate prior substeps. In (A1), $\overline{A}_i^{*}$ is the *average* breaker impulse defined as a time and space integral of the breaker function (3.11) averaged to the LES gridpoint $(\boldsymbol{x}, t)$. For example, in the x-component of the current equations,

$$\overline{A}_1^{*}(\boldsymbol{x}, t) = \frac{1}{\Delta V \ \Delta t} \int_{t}^{t+\Delta t} \int_{z-\Delta z/2}^{z+\Delta z/2} \int_{y-\Delta y/2}^{y+\Delta y/2} \int_{x-\Delta x/2}^{x+\Delta x/2} \overline{\mathscr{A}}(\alpha, \beta, \delta, \gamma) \cos\Theta \, \mathrm{d}x \, \mathrm{d}y \, \mathrm{d}z \, \mathrm{d}t \,, \tag{A2}$$

where the averaging is over the small volume $\Delta V = \Delta x \, \Delta y \, \Delta z$ and time increment Δt, and Θ is the breakers horizontal orientation in the LES grid. The integrand contains complex dependences on $(\boldsymbol{x}, t)$ because of the breaker functional forms (3.11) and (3.12) and thus the integrals in (A2) are evaluated using a trapezoidal rule on a fine mesh between LES gridpoints. The implementation evaluates (A2) at every substep at each LES gridpoint $(\boldsymbol{x}, t)$ for all active breaking events. Tests of the numerical implementation show that it conserves the total momentum from a breaker irrespective of its time and space scale and hence even small scale breakers are 'felt' in the LES grid.

In our simulations the maximum allowable timestep Δt is picked based on the grid resolution, the maximum velocity in the computational domain and a fixed CFL number. This method is adaptive at each timestep and is a robust scheme

https://doi.org/10.1017/S002211200700897X Published online by Cambridge University Press

for determining an optimum timestep for a variety of flows. Simulation diagnostics show breaking impacts the numerical stability of the code. Large breakers boost the magnitude of the work term W in the SGS e-equation (4.1), which in turn locally enhances the SGS eddy viscosity for momentum and scalars (ν_t, ν_h). To maintain numerical stability a minimum timestep is chosen to satisfy a CFL constraint or a viscous stability criterion based on the subgrid-scale eddy viscosities and grid spacing, e.g. $\Delta t < \Delta z^2/2\nu_h$ (Ferziger & Perić 2002), whichever is more stringent.

A.2. *Algorithm outline*

A synopsis of the algorithmic components of our OBL LES is the following:

(1) Select a wind speed U_a.

(a) Compute the available atmospheric momentum and energy using bulk formulas (2.5) and (2.7).

(b) Integrate the wave spectrum (2.1) to generate a vertical profile of the Stokes drift (2.4).

(c) Compute the breaker PDF and rate of breaker generation $\dot{N}$ using (3.16) and (3.17), respectively.

(d) Based on the LES grid resolution, partition the atmospheric momentum and energy fluxes into resolved and subgrid breakers as in (4.6) and (4.7).

(2) Integrate the LES equations (4.1) forward in time. Breakers obey the following rules at each full Runge–Kutta time step:

(a) Draw breaker speeds from the PDF and use the linear dispersion relation to establish other event properties.

(b) Candidate breakers are sorted by size so that the largest breakers are added to the water surface first. Small breakers fill in the remaining empty voids.

(c) Breaking events are initiated at non-overlapping surface sites drawn from a uniform random distribution.

(d) Generate the four-dimensional breaker impulse functions for each c and average the breaker impulses to the LES grid. Add breaker acceleration and work terms to the LES governing equations.

(e) Maintain and update the link list of breaking events allowing old breakers to die, existing breakers to evolve, and new breakers to be born.

REFERENCES

Alves, J. G. M., Banner, M. L. & Young, I. R. 2003 Revisiting the Pierson–Moskowitz asymptotic limits for fully developed wind waves. *J. Phys. Oceanogr.* **33**, 1301–1323.

Ardhuin, F. & Jenkins, A. D. 2006 On the interaction of surface waves and upper ocean turbulence. *J. Phys. Oceanogr.* **36**, 551–557.

Armfield, S. & Street, R. 1999 The fractional step method for the Navier–Stokes equations on staggered grids: The accuracy of three variations. *J. Comput. Phys.* **153**, 660–665.

Banner, M. L. 1990 Equilibrium spectra of wind waves. *J. Phys. Oceanogr.* **20**, 966–984.

Banner, M. L. & Peirson, W. L. 1998 Tangential stress beneath wind-driven air–water interfaces. *J. Fluid Mech.* **364**, 115–145.

Belcher, S. E. & Vassilicos, J. C. 1997 Breaking waves and the equilibrium range of wind–wave spectra. *J. Fluid Mech.* **342**, 377–401.

Chini, G. P. & Leibovich, S. 2003 Resonant Langmuir-circulation internal-wave interaction. Part 1. Internal wave reflection. *J. Fluid Mech.* **495**, 35–55.

Craig, P. D. & Banner, M. L. 1994 Modeling wave-enhanced turbulence in the ocean surface layer. *J. Phys. Oceanogr.* **24**, 2546–2559.

Craik, A. D. D. & Leibovich, S. 1976 A rational model for Langmuir circulations. *J. Fluid Mech.* **73**, 401–426.

https://doi.org/10.1017/S002211200700897X Published online by Cambridge University Press

Csanady, G. T. 1994 Vortex pair model of Langmuir circulation. *J. Mar. Res.* **52**, 559–581.

Donelan, M. A. 1998 Air–water exchange processes. In *Physical Processes in Lakes and Oceans*, *Coastal and Estuarine Studies*, vol. 54, pp. 19–36. American Geophysical Union.

Donelan, M. A. 2001 A nonlinear dissipation function due to wave breaking. In *Workshop on Ocean Wave Forcasting*. European Centre for Medium Range Weather Forecasting, Reading, England.

Donelan, M. A., Hamilton, J. & Hui, W. H. 1985 Directional spectra of wind-generated waves. *Phil. Trans. R. Soc. Lond.* A **315**, 509–562.

Donelan, M. A., Haus, B. K., Reul, N., Plant, W. J., Stiassnie, M., Graber, H. C., Brown, O. B. & Saltzman, E. S. 2004 On the limiting aerodynamic roughness of the ocean in very strong winds. *Geophys. Res. Lett.* **31**, L18306.

Donelan, M. A., Longuet-Higgins, M. S. & Turner, J. S. 1972 Whitecaps. *Nature* **239**, 449–451.

Donelan, M. A. & Pierson, W. J. 1987 Radar scattering and equilibrium ranges in wind generated waves with applications to scatterometry. *J. Geophys. Res.* **92**, 4971–5029.

Drennan, W. M., Donelan, M. A., Terray, E. A. & Katsaros, K. B. 1996 Oceanic turbulence dissipation measurements in SWADE. *J. Phys. Oceanogr.* **26**, 808–815.

Emanuel, K. 2004 Tropical cyclone energetics and structure. In *Atmospheric Turbulence and Mesoscale Meteorology* (ed. E. Fedorovich, R. Rotunno & B. Stevens), pp. 165–191. Cambridge University Press.

Emanuel, K. A. 1999 Thermodynamic control of hurricane intensity. *Nature* **401**, 665–669.

Enstad, L. I., Nagaosa, R. & Alendal, G. 2006 Low shear turbulence structures beneath stress-driven interface with neutral and stable stratification. *Phys. Fluids* **18**, 055106–1 055106–23.

Fairall, C. W., Bradley, E. F., Hare, J. E., Grachev, A. A. & Edson, J. B. 2003 Bulk parameterization of air–sea fluxes: Updates and verification for the COARE algorithm. *J. Clim.* **16**, 571–591.

Ferziger, J. H. & Perić, M. 2002 *Computational Methods for Fluid Dynamics*, 3rd edn. Springer.

Gargett, A., Tejada-Martínez, A. E. & Grosch, C. E. 2004 Langmuir supercells: A mechanism for sediment resuspension and transport in shallow seas. *Science* **306**, 1925–1928.

Gemmrich, J. R. 2005 On the occurrence of wave breaking. In *14th 'Aha Huliko'a Hawaiian Winter Workshop on Rogue Waves*, pp. 123–130. Office of Naval Research.

Gemmrich, J. R. & Farmer, D. M. 1999 Near-surface turbulence and thermal structure in a wind-driven sea. *J. Phys. Oceanogr.* **29**, 480–499.

Hara, T. & Belcher, S. E. 2002 Wind forcing in the equilibrium range of wind–wave spectra. *J. Fluid Mech.* **470**, 223–245.

Kantha, L. H. & Clayson, C. A. 2004 On the effect of surface gravity waves on mixing in the oceanic mixed layer. *Ocean Modelling* **6**, 101–124.

Kawamura, T. 2000 Numerical investigation of turbulence near a sheared air-water interface. Part 2: Interaction of turbulent shear flow with surface waves. *J. Mar. Sci. Technology* **5**, 161–175.

Kenyon, K. E. 1969 Stokes drift for random gravity waves. *J. Geophys. Res.* **74**, 6991–6994.

Klemp, J. & Durran, D. 1983 An upper boundary condition permitting internal gravity wave radiation in numercal mesoscale models. *Mon. Wea. Rev.* **11**, 430–444.

Komen, G. J., Cavaleri, L., Donelan, M., Hasselmann, K., Hasselmann, S. & Janssen, P. A. E. M. 1994 *Dynamics and Modelling of Ocean Waves*. Cambridge University Press.

Lamarre, E. & Melville, W. K. 1991 Air entrainment and dissipation in breaking waves. *Nature* **351**, 469–472.

Large, W. G., McWilliams, J. C. & Doney, S. C. 1995 Oceanic vertical mixing: A review and a model with a nonlocal boundary layer parameterization. *Rev. Geophys.* **32**, 363–403.

Large, W. G. & Pond, S. 1982 Sensible and latent heat flux measurements over the ocean. *J. Phys. Oceanogr.* **12**, 464–484.

Leibovich, S. 1983 The form and dynamics of Langmuir circulations. *Ann. Rev. Fluid Mech.* **15**, 391–427.

Lewis, D. M. & Belcher, S. E. 2004 Time-dependent, coupled, Ekman boundary layer solutions incorporating Stokes drift. *Dyn. Atmos. Oceans* **37**, 313–351.

Li, M., Garrett, C. & Skyllingstad, E. 2005 A regime diagram for classifying turbulent large eddies in the upper ocean. *Deep-Sea Res. I* **52**, 259–278.

Lin, C.-L., McWilliams, J. C., Moeng, C.-H. & Sullivan, P. P. 1996 Coherent structures and dynamics in a neutrally stratified planetary boundary layer flow. *Phys. Fluids* **8**, 2626–2639.

https://doi.org/10.1017/S002211200700897X Published online by Cambridge University Press

Liu, W. T., Katsaros, K. B. & Businger, J. A. 1979 Bulk parameterization of air–sea exchanges in heat and water vapor including the molecular constraints at the interface. *J. Atmos. Sci.* **36**, 1722–1735.

Loewen, M. R. & Melville, W. K. 1990 Microwave backscatter and acoustic radiation from breaking waves. *J. Fluid Mech.* **2**, 297–299.

Longuet-Higgins, M. S. 1975 Integral properties of periodic gravity waves of finite amplitude. *Proc. Roy. Soc. Lond.* A **342**, 157–174.

Makin, V. K., Kudryavtsev, V. N. & Mastenbroek, C. 1995 Drag of the sea surface. *Boundary-Layer Met.* **73**, 159–182.

McWilliams, J. C. 1996 Modeling the oceanic general circulation. *Annu. Rev. Fluid Mech.* **28**, 215–248.

McWilliams, J. C. & Huckle, E. 2006 Ekman layer rectification. *J. Phys. Oceanogr.* **36**, 1646–1659.

McWilliams, J. C. & Restrepo, J. M. 1999 The wave-driven ocean circulation. *J. Phys. Oceanogr.* **29**, 2523–2540.

McWilliams, J. C., Restrepo, J. R. & Lane, E. M. 2004 An asymptotic theory for the interaction of waves and currents in shallow coastal water. *J. Fluid Mech.* **511**, 135–178.

McWilliams, J. C. & Sullivan, P. P. 2000 Vertical mixing by Langmuir circulations. *Spill Sci. Technol. Bull.* **6**, 225–237.

McWilliams, J. C., Sullivan, P. P. & Moeng, C-H. 1997 Langmuir turbulence in the ocean. *J. Fluid Mech.* **334**, 1–30.

Mellor, G. L. & Yamada, T. 1982 Development of a turbulence closure model for geophysical fluid problems. *Rev. Geophys.* **20**, 851–875.

Melsom, A. & Sætra, Ø. 2004 Effects of wave breaking on the near-surface profiles of velocity and turbulent kinetic energy. *J. Phys. Oceanogr.* **34**, 490–504.

Melville, W. K. 1994 Energy dissipation by breaking waves. *J. Phys. Oceanogr.* **24**, 2041–2049.

Melville, W. K. 1996 The role of wave breaking in air–sea interaction. *Ann. Rev. Fluid Mech.* **28**, 279–321.

Melville, W. K. & Matusov, P. 2002 Distribution of breaking waves at the ocean surface. *Nature* **417**, 58–63.

Melville, W. K., Veron, F. & White, C. J. 2002 The velocity field under breaking waves: coherent structures and turbulence. *J. Fluid Mech.* **454**, 203–233.

Moeng, C-H. 1984 A large-eddy simulation model for the study of planetary boundary-layer turbulence. *J. Atmos. Sci.* **41**, 2052–2062.

Moeng, C-H. & Rotunno, R. 1990 Vertical velocity skewness in the buoyancy-driven boundary layer. *J. Atmos. Sci.* **47**, 1149–1162.

Moeng, C. H. & Wyngaard, J. C. 1989 Evaluation of turbulent transport and dissipation closures in second-order modeling. *J. Atmos. Sci.* **46**, 2311–2330.

Nepf, H. M., Cowen, E. A., Kimmel, S. J. & Monismith, S. G. 1995 Longitudinal vortices beneath breaking waves. *J. Geophys. Res.* **100**, 16,211–16,221.

Noh, Y., Min, H. S. & Raasch, S. 2004 Large eddy simulation of the ocean mixed layer: The effects of wave breaking and Langmuir circulation. *J. Phys. Oceanogr.* **34**, 720–735.

Phillips, O. M. 1977 *Dynamics of the Upper Ocean*. Cambridge University Press.

Phillips, O. M. 1985 Spectral and statistical properties of the equilibrium range in wind-generated gravity waves. *J. Fluid Mech.* **156**, 505–531.

Phillips, W. R. C. 2002 Langmuir circulations beneath growing or decaying surface waves. *J. Fluid Mech.* **469**, 317–342.

Pierson, W. J. & Moskowitz, L. 1964 A proposed spectral form for fully developed wind seas based on the similarity theory of S. A. Kitaigorodskii. *J. Geophys. Res.* **69**, 5181–5190.

Polton, J. A., Lewis, D. M. & Belcher, S. E. 2004 The role of wave-induced Coriolis–Stokes forcing on the wind-driven mixed layer. *J. Phys. Oceanogr.* **34**, 2345–2358.

Powell, M. D., Vickery, P. J. & Reinhold, T. A. 2003 Reduced drag coefficient for high wind speeds in tropical cyclones. *Nature* **422**, 279–283.

Price, J. F., Weller, R. A. & Pinkel, R. 1986 Diurnal cycling: Observations and models of the upper ocean response to diurnal heating, cooling, and wind mixing. *J. Geophys. Res.* **91**, 8411–8427.

Rapp, R. J. & Melville, W. K. 1990 Laboratory measurements of deep-water breaking waves. *Phil. Trans. R. Soc. Lond.* A **331**, 735–800.

https://doi.org/10.1017/S002211200700897X Published online by Cambridge University Press

Rascale, N., Ardhuin, F. & Terray, E. A. 2006 Drift and mixing under the ocean surface: A coherent one-dimensional description with application to unstratified conditions. *J. Geophys. Res.* **111**, C03016.

Scotti, A., Meneveau, C. & Lilly, D. K. 1993 Generalized Smagorinsky model for anisotropic grids. *Phys. Fluids* A **5**, 2306–2308.

Skyllingstad, E. 2005 Langmuir circulation. In *Marine Turbulence: Theories, Observations, and Models* (ed. H. Z. Baumert, J. Simpson & J. Sündermann), pp. 277–282. Cambridge University Press.

Skyllingstad, E. D. & Denbo, D. W. 1995 An ocean large-eddy simulation of Langmuir circulations and convection in the surface mixed layer. *J. Geophys. Res.* **100**, 8501–8522.

Smyth, W. D., Skyllingstad, E. D., Crawford, G. B. & Wijesekera, H. 2002 Nonlocal fluxes and Stokes drift effects in the K-profile parameterization. *Ocean Dyn.* **52**, 104–115.

Sullivan, P. P., McWilliams, J. C. & Melville, W. K. 2004 The oceanic boundary layer driven by wave breaking with stochastic variability. I: Direct numerical simulations. *J. Fluid Mech.* **507**, 143–174.

Sullivan, P. P., McWilliams, J. C. & Melville, W. K. 2005 Surface waves and ocean mixing: Insights from numerical simulations with stochastic surface forcing. In *14th 'Aha Huliko'a Hawaiian Winter Workshop on Rogue Waves*, pp. 147–154.

Sullivan, P. P., McWilliams, J. C. & Moeng, C-H. 1994 A subgrid-scale model for large-eddy simulation of planetary boundary-layer flows. *Boundary-Layer Met.* **71**, 247–276.

Sullivan, P. P., McWilliams, J. C. & Moeng, C-H. 1996 A grid nesting method for large-eddy simulation of planetary boundary layer flows. *Boundary-Layer Met.* **80**, 167–202.

Sullivan, P. P., Moeng, C-H., Stevens, B., Lenschow, D. H. & Mayor, S. D. 1998 Structure of the entrainment zone capping the convective atmospheric boundary layer. *J. Atmos. Sci.* **55**, 3042–3064.

Terray, E. A., Donelan, M. A., Agrawal, Y. C., Drennan, W. M., K. K. Kahma, A. J. Williams 3rd, Hwang, P. A. & Kitaigorodskii, S. A. 1996 Estimates of kinetic energy dissipation under breaking waves. *J. Phys. Oceanogr.* **26**, 792–807.

Terray, E. A., Drennan, W. M. & Donelan, M. A. 1999 The vertical structure of shear and dissipation in the ocean surface layer. In *Proc. Symp. on the Wind-Driven Air–Sea Interface—Electromagnetic and Acoustic Sensing, Wave Dynamics, and Turbulent Fluxes*, pp. 239–245. University of New South Wales, Sydney Australia.

Thorpe, S. A. 2004 Langmuir circulation. *Ann. Rev. Fluid Mech.* **36**, 55–79.

Thorpe, S. A. 2005 *The Turbulent Ocean*. Cambridge University Press.

Tsai, W-T. 1998 A numerical study of the evolution and structure of a turbulent shear layer under a free surface. *J. Fluid Mech.* **354**, 239–276.

Tsai, W-T. & Yue, D. K. P. 1996 Computation of nonlinear free-surface flows. *Ann. Rev. Fluid Mech.* **28**, 249–278.

Wu, J. 1983 Sea-surface drift currents induced by wind and waves. *J. Phys. Oceanogr.* **13**, 1441–1451.

Wu, J. 1988 Variations of whitecap coverage with wind stress and water temperature. *J. Phys. Oceanogr.* **18**, 1448–1453.

Zhou, H. 1999 Numerical simulation of Langmuir circulations in a wavy domain and its comparison with the Craik-Leibovich theory. PhD thesis, Stanford University.

https://doi.org/10.1017/S002211200700897X Published online by Cambridge University Press